Thesis for the degree of Licentiate of Engineering

Parametrically pumped superconducting circuits

Philip Krantz

Quantum Device Physics Laboratory
Department of Microtechnology and Nanoscience (MC2)
CHALMERS UNIVERSITY OF TECHNOLOGY
Göteborg, Sweden 2013

Parametrically pumped superconducting circuits
Philip Krantz

Chalmers University of Technology
Department of Microtechnology and Nanoscience - MC2
Quantum Device Physics Laboratory
SE–412 96 Göteborg, Sweden
Telephone: +46 (0)31-772 1000

ISSN 1652-0769
Technical Report MC2 - 261

Printed by Chalmers reproservice, Chalmers University of Technology
Göteborg, Sweden, October 2013

Parametrically pumped superconducting circuits
PHILIP KRANTZ
Department of Microtechnology and Nanoscience
Chalmers University of Technology
Göteborg, Sweden 2013

Abstract

In this licentiate thesis, I present the design, fabrication, and characterization of superconducting parametric resonators, for use in quantum information processing.

These devices are quarter-wavelength coplanar waveguide resonators ($\approx$ 5 GHz), terminated at one end by a non-linear inductance provided by a SQUID (superconducting quantum interference device). The SQUID acts as a flux-controlled boundary condition, which effectively changes the electrical length of the resonator. This enables the modulation of the resonant frequency by coupling microwave magnetic flux into the SQUID, using on-chip transmission lines. The modulation occurs on a timescale much faster than the photon loss out of the resonator.

The non-linearity provides several different regimes for operating this device. I focused on the parametric regime, in which the non-linear element was being modulated (pumped) at or near twice the resonant frequency. This pumping can lead to amplification and frequency conversion of an incoming signal. It can also give rise to instabilities and self-oscillations "parametric oscillations" $-$ that is, the generation of an intense electric field in the resonator (the creation of photons). Parametric oscillations set in when the pumping strength exceeds a threshold value, and also depends on the pump-frequency detuning from twice the resonance and on the static flux through the SQUID.

I characterized the devices over a wide parameter range by doing homodyne detection of the reflected signal or of the emitted field oscillations. In particular, I investigated the damping and two leading nonlinearities, dominating in different operating regimes, which influence the dynamics of the parametric resonator.

First, I extracted the Duffing nonlinearity by studying the line width of the resonator as a function of the input signal (without pumping the SQUID). Second, with high pump amplitude, I extracted the pump-induced nonlinearity by determining the threshold parameters (pump

amplitude and detuning) for the onset of parametric oscillations; this nonlinearity leads to the generation of higher-order pump terms that complicate the system dynamics, but can be mitigated now that they have been understood. My results validate a recent theoretical model for the classical, non-linear dynamics of parametric resonance, and helps determine workable design parameters.

Finally, I helped develop a linearized model − the "pumpistor" − describing this device in terms of a flux-controlled impedance. This will be useful when designing more complex circuits.

One goal of this work is to demonstrate single-shot measurements on superconducting qubits (quantum bits of information). We will use the parametric resonator as a threshold discriminator, associating the qubit's two energy eigenstates with the parametric oscillations either turning on or not. This would be a very useful device in the quantum engineer's toolbox when designing systems for quantum information processing and communication.

Keywords: Superconducting circuits, resonators, parametric oscillators, Josephson junction, SQUID, quantum bit, quantum information, circuit quantum electrodynamics, pumpistor

List of appended publications

This thesis is based on the work contained in the following papers:

I. **Investigation of nonlinear effects in Josephson parametric oscillators used in circuit QED**
P. Krantz, Y. Reshitnyk, W. Wustmann, J. Bylander, S. Gustavsson, W. D. Oliver, T. Duty, V. Shumeiko, and P. Delsing
New Journal of Physics **15**, in press (2013).

II. **The pumpistor: a linearized model of a flux-pumped superconducting quantum interference device for use as a negative-resistance parametric amplifier**
K.M. Sundqvist, S. Kintaş, M. Simoen, **P. Krantz**, M. Sandberg, C.M. Wilson, and P. Delsing
Appl. Phys. Lett. **103**, 102603 (2013).

Papers outside of the scope of this thesis

III. **Fabrication of large dimension aluminum air-bridges for superconducting quantum circuits**
M. Abuwasib, **P. Krantz**, and P. Delsing
J. Vac. Sci. Technol. B **31**, 031601 (2013).

IV. **Coupling of an erbium spin ensemble to a superconducting resonator**
M. U. Staudt, I-C Hoi, **P. Krantz**, M. Sandberg, M. Simoen, P. Bushev, N. Sangouard, M. Afzelius, V. S. Shumeiko, G. Johansson, P. Delsing, and C. M. Wilson
J. Phys. B: At. Mol. Opt. Phys. **45**, 124019 (2012).

V. **An On-Chip Mach-Zehnder Interferometer in the Microwave Regime**
S. Schuermans, M. Simoen, M. Sandberg, **P. Krantz**, C. M. Wilson, and P. Delsing
IEEE Trans. on Appl. Supercond. **21**, no. 3 (2011).

Acknowledgements

The work contained in this thesis would not have been possible without the assistance and support from many people. First of all, I would like to express my sincere gratitude to my supervisor and examiner Prof. Per Delsing for giving me the opportunity to carry out my doctoral studies in his group. Per is a very motivating and inspiring leader, who always has an open door and mind for discussing new ideas and providing important guidance. Second, I would like to thank my co-supervisors Prof. Chris Wilson and Ass. Prof. Jonas Bylander for many inspiring discussions about low-temperature physics and measurement techniques. Thank you Jonas for taking me on as a visiting student at MIT last year where I learned a lot about measurement techniques.

Thank you Arsalan Pourkabirian and Michaël Simoen for being the best possible friends, both in the office and outside. Many thanks goes all the people at QDP for creating a nice work environment: Mathieu Pierre, Matthias Staudt, Martin Gustafsson, Thomas Aref, Samuel Lara Avila, André Dankert, Io-Chun Hoi, Seckin Kintas, Sebastian de Graaf, Niclas Lindvall, Kyle Sundqvist, Ida-Maria Svensson, Maria Ekström, Astghik Adamyan, Thilo Bauch, Sophie Charpentier, Simon Abay Gerbrehiwot, Thomas Yager, Andrey Danilov, Samuel Lara Avila, Saroj Prasad Dash, Sergey Kubatkin, Arseniy Lartsev, Avgust Yurgens, Jan Jacobsson, Staffan Pehrson, Lars Jönsson, Maria Tremblay, and Susannah Carlsson.

I am also very grateful for all the theory discussions I had with the people at Applied Quantum Physics laboratory: Vitaly Shumeiko, Waltraut Wustmann, Göran Johansson, and Lars Tornberg. Without all of you, I would not know much about our measured devices. Many thanks goes to the staff of the Nanofabrication laboratory for all the processing related assistance, especially Henrik Frederiksen and Kaija Matikainen.

In addition to all of you mentioned above, there are several people with whom we got the honor to collaborate: The group at Massachusetts Institute of Technology: Terry Orlando, Will Oliver, Simon Gustavsson, Xiaoyue Jin, and Fei Yan. The group at University of New South Wales and University of Queensland in Australia: Tim Duty, Yarema Rushitnyk, and Jean-Loup Smirr. The Microscopy group at Chalmers: Samira Nik, Lunjie Zeng, and Eva Olsson.

Finally, all my love to my family: Sören, Inger, Linda, Henrik, and Tove as well as to my wonderful girlfriend Eli. Thank you so much for all your support and for always being there for me. Without you, I would not be where I am today!

Philip Krantz
Göteborg, October, 2013

List of symbols

Constants

$\hbar$	Reduced Planck constant	$h/2\pi \approx 1.1 \times 10^{-34}$ Js
e	Elementary charge	$\approx 1.6 \times 10^{-19}$ C
c	Speed of light in vacuum	$\approx 3 \times 10^{8}$ m/s
k_{B}	Boltzmanns constant	$\approx 1.4 \times 10^{-23}$ J/K
Φ_0	Magnetic flux quantum	$h/2e \approx 2.0 \times 10^{-15}$ Wb
R_{Q}	Quantum of resistance	$h/(4e^2) = R_K/4 \approx 6.5\mathrm{k}\Omega$

Chapter 1: Introduction

$\psi(\mathbf{r})$	Superconducting wave function
$\varphi(\mathbf{r})$	Phase of the superconducting wavefunction
$\rho(\mathbf{r})$	Pair density
I_{c}	Critical current of Josephson junction
φ	Phase difference across Josephson junction ($\varphi_1 - \varphi_2/2$)
Φ_{dc}	dc magnetic flux
Φ_{ac}	ac magnetic flux
L_{s}^0	Inductance of SQUID at zero-flux and bias ($\Phi_0/(2\pi I_c)$)
γ	Complex propagation constant
Z_{c}	Characteristic impedance ($\sqrt{L/C}$)
v_{ph}	Phase velocity ($1/\sqrt{LC}$)
g,w	Gap and center conductor width of CPW
l	Length of resonator
λ	Wavelength of resonator

Chapter 2: Theory

The tunable resonator

C_{c}	Coupling capacitor
f_0	Resonance frequency ($\omega_0/2\pi$)
ϵ_{eff}	Effective dielectric constant
S_{11}	Complex reflection coefficient ($\lvert S_{11}\rvert \mathrm{e}^{i\arg(S_{11})}$)
Q_{i}	Internal quality factor
Q_{e}	External quality factor
Q_{tot}	Total quality factor ($(1/Q_{\mathrm{i}} + 1/Q_{\mathrm{e}})^{-1} = \omega_r/2\Gamma$)
δf	Probe$-$resonator detuning ($f - f_0$)
F	dc flux bias ($\pi\Phi_{\mathrm{dc}}/\Phi_0$)
γ_0	Inductive participation ratio (L_{s}^0/Ll)
$\omega_{\lambda/4}$	Bare angular resonator frequency
ω_p	Parametric angular pump frequency

The parametric oscillator

Φ_i	Canonical flux at node i
ϵ	Pump amplitude
ϵ'	Normalized pump amplitude ($\epsilon Q_\mathrm{tot}/\omega_r\omega_p$)
δ	Pump−resonator detuning ($\omega_p/2-\omega_r$)
δ'	Normalized pump−resonator detuning (δ/Γ)
α	Duffing nonlinearity parameter
α'	Normalized Duffing parameter ($3\alpha/4\Gamma\omega_p$)
q_1,q_2	In-phase and quadrature voltages
g	Parametric voltage gain
β	Pump−induced nonlinearity parameter
θ_p,θ_s	Pump and signal phases
$\Delta\theta$	Phase angle between pump and signal ($2\theta_s-\theta_p$)

The transmon qubit

C_g	Gate capacitance
C_s	Shunt capacitance
C_J	Josephson capacitance
C_Σ	Total qubit capacitance ($C_\mathrm{g}+C_\mathrm{s}+C_\mathrm{J}$)
V_g	Gate voltage
Δ	Superconducting gap (1.76 k_BT_c)
n_g	Reduced gate charge ($C_\mathrm{g}V_\mathrm{g}/2e$)
E_c	Charging energy ($e^2/2C_\Sigma$)
E_J	Josephson energy ($\Phi_0 I_\mathrm{c}/2\pi$)
R_n	Normal state resistance
$\|0\rangle$,$\|1\rangle$	Ground- and first excited qubit states
ω_a	Qubit transition frequency
α_r	Relative anharmonicity ($(E_{12}-E_{01})/E_{01}$)
$\hat{\sigma}_z$	Pauli's z-matrix ($\|0\rangle\langle 0\| - \|1\rangle\langle 1\|$)
$\hat{a}^\dagger$,$\hat{a}$	Creation and annihilation operators
$\hat{\sigma}_+$,$\hat{\sigma}_-$	Atomic transition operators ($\|1\rangle\langle 0\|, \|0\rangle\langle 1\|$)
$\hat{n}$	Photon number operator ($\hat{a}^\dagger\hat{a}$)
g	Qubit−resonator coupling rate
Ω_R	Vacuum Rabi frequency ($\sqrt{n}g/\pi$)
Δ	Qubit−resonator detuning ($\omega_a-\omega_r$)

Chapter 3: Experiments

P_{ox}	Oxidation pressure
t_{ox}	Oxidation time
η	Evaporation angle

Chapter 4: Results

A	Intra−resonator field amplitude ($\|A\|^2$ number of photons)
B	Resonator probe field ($\|B\|^2$ has units of photons/s)
C	Outgoing field ($\|C\|^2$ has units of photons/s)

List of abbreviations

cQED	circuit Quantum ElectroDynamics
Qubit	Quantum bit
SQUID	Superconducting QUantum Interference Device
SEM	Scanning Electron Microscope
CPW	Coplanar Waveguide
TEM	Transverse Electromagnetic
CPB	Cooper Pair Box
CNC	Computer Numerical Control
PCB	Printed Circuit Board

Table of Contents

Chapter 1

Introduction

1.1 Motivation

In 1982, R. P. Feynman[1] suggested an alternative to using "classical" computers when simulating and solving problems of quantum mechanical nature. He argued that quantum systems could be modeled with much greater efficiency by using a processor whose architecture, in itself, is based on the laws of quantum mechanics. This was the starting point for the quest of the so-called *quantum computer*, where quantum information would be encoded into quantum bits (qubits). By utilizing the superposition and entanglement properties associated with quantum objects, this processor would be able to perform parallel operations, offering new ways to substantially increase the processing power compared with its classical counterpart.

Even though several algorithms have been created for quantum computation, the development of its hardware has proven to be a big challenge. The practical obstacle is due to the issue of isolating qubits from their environment, while maintaining control to coherently manipulate them. In fact, the field of quantum information technology has gradually evolved into an engineering field of research where experimental advances are used to continuously benchmark various hardware architectures against each other.

In this work, we utilize circuit Quantum Electrodynamics (cQED)[2, 3], where superconducting circuits fabricated on-chip using microfabrication techniques are used as a platform for processing quantum information. One advantage of using lithographically defined circuit elements as compared to other qubit implementations is their potential of scalability, to integrate a large number of qubits together. Another very important aspect of quantum computation is to be able to read out the state of a qubit with good fidelity and on a short time-scale, compared with the quantum coherence time of the system. A commonly used method is dispersive read-out, where the qubit is coupled to a superconducting resonator, which resonant frequency is slightly dependent on the state of the qubit.

The long term goal of this work is to develop a single shot readout, where the state of the qubit is mapped onto the dynamics of a parametric oscillator. This thesis outlines the properties of a parametric oscillator based on a tunable superconducting resonator. The resonator is parametrically driven by modulating its resonant frequency at a rate of twice its resonant frequency.

1.2 Superconductivity

In 1911, H. K. Onnes[4] made a ground breaking discovery in physics. He concluded that the electrical resistance of mercury abruptly dropped by several orders of magnitude when the metal was cooled below a critical temperature, T_c. This phenomenon, now known as *superconductivity* turned out to be true also for many other metals, only at different critical temperatures. In his lectures on physics, Feynman discusses in short terms the origin to why superconductivity is observed for many metals [5]. The interaction between the electrons in the metal and the vibrations of its atom lattice (phonons) give rise to small effective attraction between the electrons. Therefore, it is energetically favorable for them to form pairs. This has the remarkable effect that the electrons, which are Fermi particles, will become Bose particles (bosons) as they appear in such a pair with a total spin of 1. The electron pairs, known as Cooper-pairs, carry the property that if a large number of pairs are occupying the same energy state, so will nearly all other pairs since Pauli's exclusion principle does not apply to the bosons. Now, due to the fact that the superconducting state of a metal takes place at very low temperatures, almost all Cooper-pairs will be bound to stay in their lowest energy state. The Cooper-pair bonds are, however, very weak and are therefore easily broken if only a small thermal energy acts on them. The thermal energy needed to break up the Cooper-pairs dictates the critical temperature for the superconductor at hand. The wave function of the Cooper-pairs in their lowest energy state can be written

$$\psi(\mathbf{r}) = \sqrt{\rho(\mathbf{r})}\mathbf{e}^{\mathbf{i}\varphi(\mathbf{r})}, \tag{1.1}$$

where $\rho(\mathbf{r})$ is the pair density and $\varphi(\mathbf{r})$ is the quantum mechanical phase.

The peculiar properties of superconductors that have been discovered during the past century, has opened completely new fields of research. One of the most important features is the tunneling of these Cooper-pairs through thin barriers, separating two superconductors. This element, known as the *Josephson junction*, allows for the creation of non-linear, dissipationless circuit elements and is the topic of next section. For more elaborate explanation of superconductivity, the reader is referred to textbooks on the topic, such as [6, 7].

1.2.1 The Josephson effects

Within the context of the superconducting devices presented in this thesis, as well as all other theses in circuit QED, the Josephson junction is the most fundamental building block from which most other non-linear properties originate. In 1962, about fifty years after the discovery of superconductivity, B. D. Josephson made the theoretical prediction that when two superconductors were put in close vicinity of each other, forming a weak link known as a Josephson junction, a zero-voltage tunneling current of Cooper-pairs could flow through the junction[9], see Fig. 1.1(a). In order for the tunneling to take place, the thickness of the insulating barrier needs to be thin enough for the wave functions in Eq. (1.1) of each superconducting electrode to overlap each other as they decay exponentially into the barrier, see Fig. 1.1(b). Josephson described this tunneling phenomenon in terms of two effects:

The *dc Josephson effect* relates the tunneling current, I, flowing through the junction with the phase difference, φ, across it

$$I = I_c \sin(\varphi), \tag{1.2}$$

where I_c is the critical current of the junction, *i.e.* the maximum super-current it can support before switching into its resistive branch. The *ac Josephson effect* relates the voltage across the junction, V, with the time-derivative of the phase difference

$$V = \left(\frac{\hbar}{2e}\right)\frac{d\varphi}{dt} = \left(\frac{\Phi_0}{2\pi}\right)\frac{d\varphi}{dt}, \tag{1.3}$$

where $\Phi_0 = h/(2e)$ denotes the magnetic flux quantum.

In this thesis, the Josephson junctions are implemented in a parallel pair, forming a so-called Superconducting Quantum Interference Device, (SQUID). We extend Eq. (1.2) and (1.3) to this case, see Fig. 1.1(c), with the junctions denoted "1" and "2". The first Josephson relation in (1.2) now gets modified to

$$I = I_{c1}\sin(\varphi_1) - I_{c2}\sin(\varphi_2). \tag{1.4}$$

Due to the fact that flux in the superconducting loop is quantized[7], we get the following quantization condition

$$\varphi_1 + \varphi_2 + 2\pi\frac{\Phi_{\mathrm{dc}}}{\Phi_0} = 2\pi n, \tag{1.5}$$

where n is the number of flux quantum in the loop. By choosing the case of one flux quantum, ($n = 1$), and using relations (1.4) and (1.5), the total current flowing through the two junctions can be expressed as

$$\begin{aligned} I = {} & (I_{c1} + I_{c2})\cos\left(\pi\frac{\Phi_{\mathrm{dc}}}{\Phi_0}\right)\sin\left(\frac{\varphi_1 - \varphi_2}{2}\right) - \\ & (I_{c1} - I_{c2})\sin\left(\pi\frac{\Phi_{\mathrm{dc}}}{\Phi_0}\right)\cos\left(\frac{\varphi_1 - \varphi_2}{2}\right). \end{aligned} \tag{1.6}$$

For the application throughout this thesis, the critical currents needed allow us to make the junction areas relatively large as compared with the grain size of the Aluminum. The two junctions can therefore be fabricated almost identical, yielding $I_{c1} \approx I_{c2}$. Thus, relation (1.6) reduces to only its first term

$$I = I_c \cos\left(\pi \frac{\Phi_{\mathrm{dc}}}{\Phi_0}\right) \sin(\varphi)\,, \tag{1.7}$$

where we have introduced an effective critical current $I_c = I_{c1} + I_{c2} = 2I_{c1}$ and an effective phase difference $\varphi = (\varphi_1 - \varphi_2)/2$.

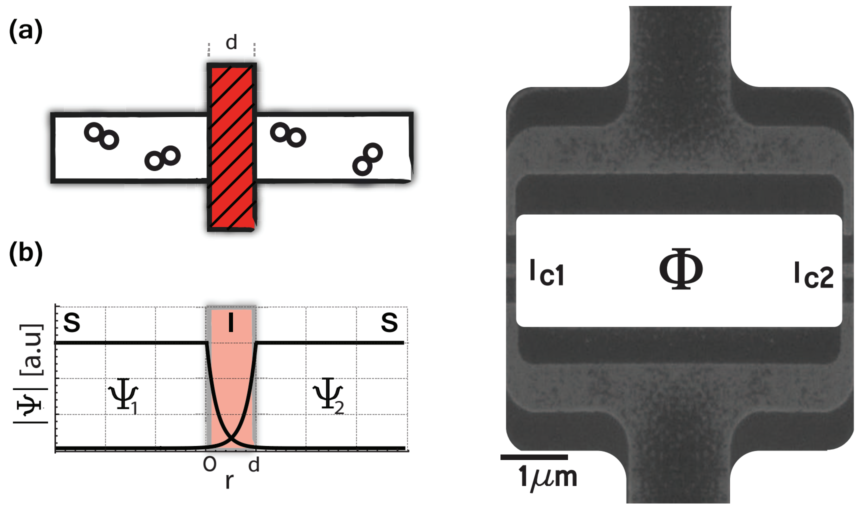

Figure 1.1: **(a)** Schematic drawing of a Josephson junction composed of two superconducting electrodes, separated by a thin insulating barrier of thickness d. **(b)** The wavefunctions of the two identical superconductors in **(a)**. The exponential decay of the wavefunctions for the electrodes have a small overlap, allowing a supercurrent to flow through the junction. **(c)** Scanning electron micrograph of an Al SQUID. The two Josephson junctions have critical currents of I_{c1} and I_{c2}, respectively. The substrate has been cut out to guide the eye.

1.2.2 The Josephson inductance

Another important feature of the Josephson junction is that it accumulates energy from the tunneling Cooper-pairs, known as *Josephson energy*, resulting in a non-linear inductance. We can derive this *Josephson inductance* of the SQUID from the time derivative of the current flowing through it

$$\frac{dI}{dt} = I_c \left|\cos\left(\pi\frac{\Phi_{\rm dc}}{\Phi_0}\right)\right| \cos(\varphi)\,\frac{d\varphi}{dt}, \tag{1.8}$$

where the absolute value of the flux term can be dropped when considering a single flux quantum. Using Eq. (1.3) and re-arranging the terms of Eq. (1.8), the voltage across the junction can be related with the time-derivative of the current

$$V = \frac{\hbar}{2e}\frac{1}{I_c\left|\cos\left(\pi\frac{\Phi_{\rm dc}}{\Phi_0}\right)\right|\cos(\varphi)}\frac{dI}{dt}. \tag{1.9}$$

Recalling that $V = L(dI/dt)$, the Josephson inductance can by identified as

$$L_s = \frac{\hbar}{2e}\frac{1}{I_c\left|\cos\left(\pi\frac{\Phi_{\rm dc}}{\Phi_0}\right)\right|\cos(\varphi)} = \frac{L_s^0}{|\cos(\pi\Phi_{\rm dc}/\Phi_0)|} \tag{1.10}$$

where $L_{\rm s}^0 = \hbar/(2eI_c) = \Phi_0/(2\pi I_c)$ is the SQUID inductance at zero applied flux and zero bias current.

1.3 Microwave theory of transmission lines

When designing a microscopic superconducting circuit, operated at microwave frequencies, an essential aspect of the work is dedicated to modelling its dimensions. The transmission lines used in this thesis are coplanar waveguides (CPW), named after its inventor C. P. Wen[10]. It resembles a flattened coaxial cable with a center conductor of width, w separated from ground planes on each side by gaps of width, g, see Fig. 1.2(a). Like the coaxial cable, the propagating microwave photons in the line give rise to Transverse Electromagnetic (TEM) waves. We can study the properties of the transmission line using the telegraph equations[11], where the transmission line is represented by a series of infinitesimally short segments of length $dz \to 0$, see Fig. 1.2(b). Each segment is composed of a distributed resistance and inductance represented by a series resistor, Rdz, and inductor, Ldz, respectively. The dielectric material separating the center conductor from the ground planes is represented by a shunt resistor with conductance, Gdz and the capacitance by a shunt capacitor, Cdz. Thus, R,L,G, and C represent the circuit quantities per unit length dz. The voltage and current at position z along the line can be written as

$$\begin{cases} V(z) = V^+ \mathrm{e}^{-\gamma z} + V^- \mathrm{e}^{\gamma z} \\ I(z) = I^+ \mathrm{e}^{-\gamma z} - I^- \mathrm{e}^{\gamma z} \end{cases}, \tag{1.11}$$

where $\gamma = \sqrt{(R + i\omega L)(G + i\omega C)}$ is the complex propagation constant at the angular microwave frequency ω. $V^\pm, I^\pm$ denote the voltage and current amplitudes of the waves travelling forward (+) and backward (-). From these, the characteristic impedance of the line can be expressed as

$$Z_c = \frac{V^+}{I^+} = \sqrt{\frac{R + i\omega L}{G + i\omega C}}. \tag{1.12}$$

For a superconducting transmission line, we can assume very small losses. Thus, the resistors can be neglected and Eq. (1.12) gets reduced to

$$Z_c \approx \sqrt{\frac{L}{C}}. \tag{1.13}$$

In addition to the magnetic inductance in the transmission line, a *kinetic inductance* due to the inertia of the paired electrons contributes if the electrode thickness, t is approaching the magnetic penetration depth of the superconducting film[7, 12]. The velocity of the propagating wave is then given by the phase velocity

$$v_{\mathrm{ph}} = \frac{1}{\sqrt{LC}}. \tag{1.14}$$

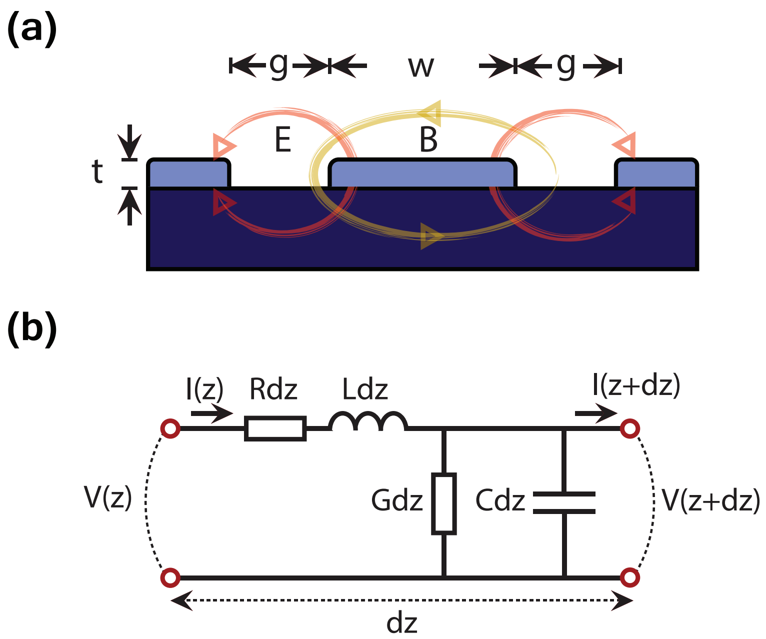

Figure 1.2: **(a)** Cross-section of a coplanar waveguide design with metal thickness t, center conductor of width w, separated to the ground planes by gaps of width g. The electric field from the center conductor to ground is marked with red, whereas the magnetic field surrounding the center conductor is marked with yellow. **(b)** Lumped-element representation of a short unit segment of the transmission line.

1.4 Circuit quantum electrodynamics

The theory of Quantum Electrodynamics (QED) was introduced by P. Dirac in the 1920s[13], and describes the interaction between electromagnetic radiation and matter. In his work, Dirac pioneered the view of the radiation and atom as a unified system and computed the coefficient of spontaneous emission of atoms, which agreed with Einstein's previously presented theory[14]. Inspired by Dirac's and Einstein's work, S-I Tomonaga[15], J. Schwinger[16], and R.P. Feynman[17] developed the theory of QED for which they were awarded the Nobel prize in physics 1965.

In nature, the interactions between individual atoms and photons are very weak due to the large mode volume of the field and small dipole moment of the atom, presenting an obstacle for studying these phenomena experimentally. This practical issue was solved as cavity QED evolved[18, 19], where Rydberg atoms with large moments are stored between two highly reflective mirrors, forming a resonant cavity with only specific frequency modes as set by the distance between the mirrors, see Fig. 1.3(a). At the resonant frequency of the cavity, an enhancement of the field inside the resonator yields a strong photon-atom coupling due to the fact that the photons get more chances to interact with the atoms. In addition, the mode structure of the resonator protects the atoms from spontaneous emission of excitations at off-resonant frequencies. These high quality resonators in combination with the large dipole moment of the Rydberg atoms thus enable the observation of coherent energy exchange between the cavity and atoms. In fact, cavity QED offers the possibility to build the hardware of a quantum processor where the computational basis is encoded into two eigenstates of the atomic energy spectrum[1]. However, in order to realize a large scale processor, it is favorable to be able to completely control and tailor the properties of the atoms as well as storing them for a long time.

In 2004, cavity QED and quantum optics technologically merged with the experimental advances of superconducting circuits fabricated using nano fabrication techniques. The result was the field of circuit QED (cQED)[2, 3], where the optical cavities were replaced with microwave resonators with resonance frequencies in the GHz-range, see Fig. 1.3(b). In turn, the atoms were replaced by mesoscopic artificial atoms with atom-like energy spectra. The quasi one-dimensional architecture of the transmission line resonators give very small mode volume. This allows the interaction between the atom and resonator to enter into the strong coupling regime, where the coupling rate is much greater than both the rate at which the photon leaves the resonator and the quantum coherence time of the artificial atom.

Circuit QED has over the past decade been proven a useful platform for realizing various building blocks needed to develop a large scale quantum computer.

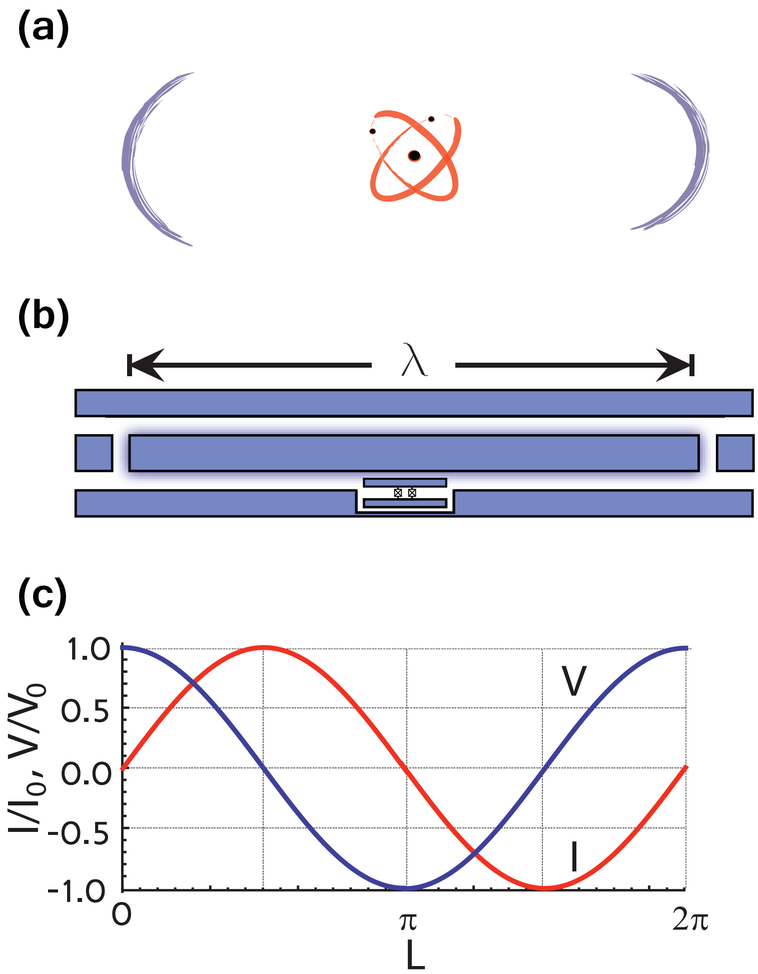

Figure 1.3: **(a)** Cartoon of cavity QED where an atom is stored in an optical cavity defined in between two highly reflective mirrors. **(b)** The corresponding picture in circuit QED, where the resonator is defined by a piece of CPW transmission line, opened in both ends.**(c)** The voltage (in blue) and current (in red) as function of position of the resonator. The artificial atom is capacitive coupled strongest to the resonator where the voltage has a maximum.

1.5 Structure of the thesis

The thesis is organized as follows: In Chapter 2, we introduce the necessary theoretical framework, starting with the construction of superconducting resonators and how these are characterized using microwave photons. In the later part of that chapter, we extend the system to the tunable resonator and introduce the notion of parametric pumping and the pumpistor model. The system can be coupled to superconducting transmon qubits, introduced in the last section of the theory chapter. There we also introduce the reader to dispersive read-out of the qubit.

In Chapter 3, the experimental aspects of the projects are outlined. Here, the reader is first introduced to the methods used to design the parametric device. Then, the main fabrication methods are described, followed by a description of the cryogenic measurement techniques used to characterize the samples.

In Chapter 4, the main results from the device characterization are presented. First, the static characterization techniques, when the resonator frequency is changed using a dc-coil. Second, the parametric character of the device is revealed using an on-chip rf line to modulate the resonant frequency of the resonator.

Finally, in Chapter 5 we conclude the work and present an outlook, discussing future directions of our research.

Chapter 2

Theory

2.1 Superconducting resonators

One of the fundamental building blocks used in circuit QED is the superconducting resonator. Throughout this thesis, we use quarter wavelength resonators, realized by a coplanar waveguide transmission line of length, $l = \lambda/4$, see Fig. 2.1(a). In one end we interrupt the center conductor and thus define a coupling capacitor, C_c, through which the resonator is probed using reflectometry measurements. In the other end, the center conductor is shorted to ground. Even though the distributed resonator has multiple modes, its fundamental resonant frequency, f_0 can be modeled using a single-mode lumped element representation of the circuit, see Fig. 2.1(b), when it is probed close to its fundamental mode frequency. The resonance frequency can be written as

$$f_0 = \lambda^{-1} v_{\mathrm{ph}} = \frac{c}{4l\sqrt{\epsilon_{\mathrm{eff}}}}, \tag{2.1}$$

where the phase velocity, $v_{\mathrm{ph}} = c/\sqrt{\epsilon_{\mathrm{eff}}}$ is expressed in terms of the effective dielectric constant ϵ_{eff}, set by the dielectric environment surrounding the resonator and the speed of light in vacuum, c.

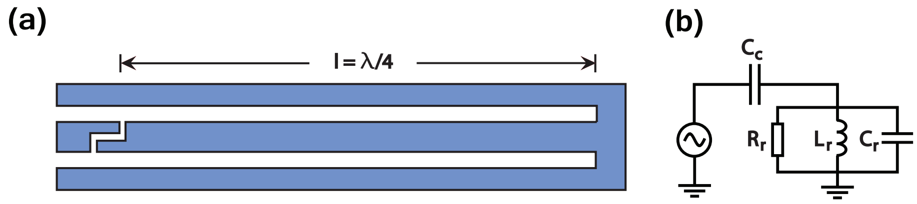

Figure 2.1: **(a)** The quarter-wavelength resonator consists of a CPW transmission line, shorted in one end and probed through a coupling capacitor, C_c, in the other. **(b)** Close to the resonant frequency, the response of the system can be modeled using a lumped element representation.

2.2 Reflected microwave response

In this section, we will briefly discuss how we can extract the fundamental properties of the resonator by fitting the measured reflected magnitude, $|S_{11}|$, and phase, $\arg(S_{11})$. For the full derivation, the reader is referred to Appendix B.

From the reflection coefficient, S_{11}, we extract the fundamental resonance frequency, f_0, and two quality factors of the system, *i.e.* the resonators ability to store energy. The total (or loaded) quality factor, Q_{tot} is defined as the ratio between stored to dissipated energy per radian. Moreover, the photon loss rate can be divided into internal loss rate $\Gamma_R = f_0/Q_i$ taking into account the photons dissipated inside the device, and external loss rate $\Gamma_0 = f_0/Q_e$ referring to the photons leaving the resonator via the coupling capacitor. The total quality factor can be expressed in terms of these two contributions as

$$Q_{\text{tot}} = \left(\frac{1}{Q_i} + \frac{1}{Q_e}\right)^{-1} \tag{2.2}$$

The starting point when deriving a fit function for the reflected response is to conclude that it is related to the impedance impedance of the lumped element circuit, Z_r and the probe line, $Z_0 \approx 50\Omega$[11] as

$$S_{11} = \frac{Z_r - Z_0}{Z_r + Z_0}, \tag{2.3}$$

where the total impedance of the coupling capacitor and the RLC resonator in Fig. 2.1(b) is given as

$$Z_r = \frac{1}{i\omega C_c} + \left(\frac{1}{R_r} + \frac{1}{i\omega L_r} + i\omega C_r\right)^{-1}. \tag{2.4}$$

After some algebra and implementation of appropriate approximations (presented in Appendix B), the complex reflection coefficient takes the form

$$S_{11} = \frac{\delta f^2 + \frac{1}{4}\left(\Gamma_R^2 - \Gamma_0^2\right) + i\Gamma_0 \delta f}{\delta f^2 + \frac{1}{4}\left(\Gamma_R + \Gamma_0\right)^2}, \tag{2.5}$$

where $\delta f = f - f_0$ denotes the detuning away from resonance. From relation (2.5), the magnitude and phase of the reflection coefficient can be derived as

$$|S_{11}| = \sqrt{\operatorname{Re}\left[S_{11}\right]^2 + \operatorname{Im}\left[S_{11}\right]^2} = \frac{\sqrt{\left(\delta f^2 + \frac{1}{4}\left(\Gamma_R^2 - \Gamma_0^2\right)\right)^2 + \left(\Gamma_0 \delta f\right)^2}}{\delta f^2 + \frac{1}{4}\left(\Gamma_R + \Gamma_0\right)^2} \tag{2.6}$$

$$\arg(S_{11}) = \arctan\left(\frac{\operatorname{Im}\left[S_{11}\right]}{\operatorname{Re}\left[S_{11}\right]}\right) = \arctan\left(\frac{\Gamma_0 \delta f}{\delta f^2 + \frac{1}{4}\left(\Gamma_R + \Gamma_0\right)^2}\right) \tag{2.7}$$

From Eq. (2.2), we see that there are three possible coupling regimes between the internal and external quality factors. If $Q_i < Q_e$, the resonator is *undercoupled* and the photons tend to get dissipated inside the resonator prior to leaking out via the coupling capacitor, see Fig. 2.2(a). When the two quality factors are matched, $Q_i = Q_e$, the resonator is *critically coupled* and the magnitude response deviates from the otherwise Lorentzian line shape and drops down to zero exactly at resonance, see Fig. 2.2(b). The third, and usually most preferred regime is when $Q_i > Q_e$ and the resonator is *overcoupled*, see Fig. 2.2(c). In this case, most photons leave the system through the coupling capacitor and can thus get detected and measured.

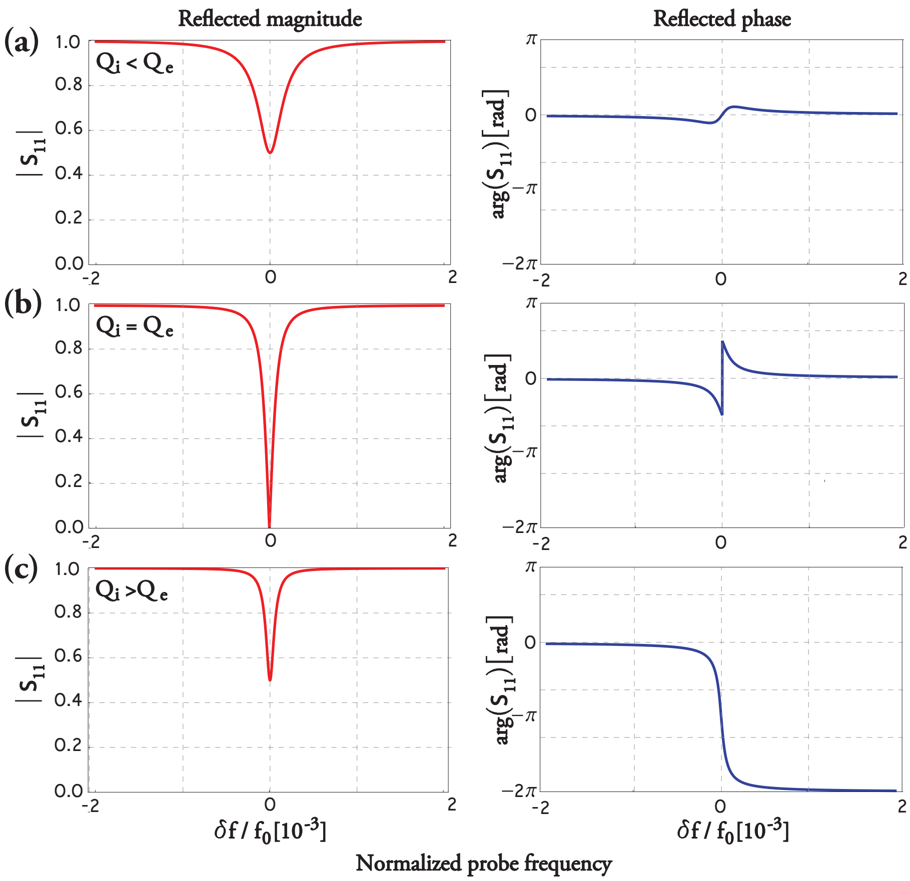

Figure 2.2: The reflected magnitude and phase responses of the quarter-wavelength resonator as a function of the normalized probe frequency in its three different coupling regimes: **(a)** undercoupled when $Q_e < Q_i$, **(b)** critically coupled when $Q_e = Q_i$, and **(c)** overcoupled when $Q_e > Q_i$.

2.3 The tunable resonator

In this work, we use an extended and well known version of the resonator where another degree of freedom is introduced by making them tunable in frequency[21, 22, 23, 24]. In the previous section 2.1, we modelled the distributed superconducting resonator as a lumped element LC-oscillator (close to its resonant frequency). Thus, a resonator with tunable frequency can be realized if either its total inductance or capacitance is tunable. Here we choose to introduce a tunable inductance by shorting the resonator to ground via two Josephson junctions in parallel, forming a SQUID[1]. The Josephson inductance will then take part in the total inductance of the resonator, with a participation ratio, $\gamma_0 \approx 5 - 10\%$, see Fig. 2.3(a). Moreover, the tuning is accomplished by threading the loop of the SQUID with magnetic flux, see Fig. 2.3. This has the consequence of tuning the electrical length of the resonator, see Fig. 2.3(b). The modulated Josephson inductance thus gets mapped onto a modulated resonant frequency, well approximated as

$$\omega_r(F) \approx \frac{\omega_{\lambda/4}}{1 + \gamma_0 / |\cos(F)|} \tag{2.8}$$

where $F = \pi\Phi_{\mathrm{dc}}/\Phi_0$ is the applied dc-flux, and $\omega_{\lambda/4} = \omega_r|_{\gamma_0=0}$ denotes the bare resonant frequency, in the absence of the Josephson contribution to its total inductance. The shape of the frequency tuning curve as a function of applied magnetic flux is governed by the participation ratio of the nonlinear Josephson inductance L_s in Eq. (1.10) to the geometrical resonator inductance, $\gamma_0 = L_s(F = 0)/Ll$, where L is the inductance per unit length of the resonator and l its length, see Fig. 2.4.

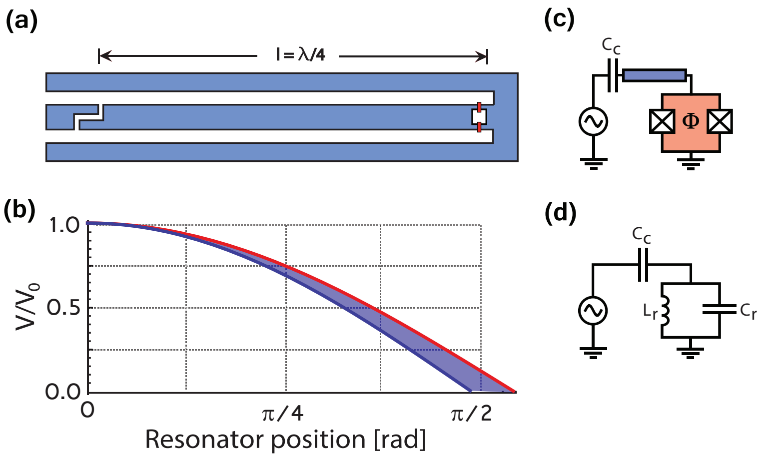

Figure 2.3: **(a)** CPW quarter-wavelength resonator, terminated to ground via a SQUID. **(b)** By changing the dc magnetic flux through the SQUID, the electrical length of the resonator is varied, yielding a modified fundamental frequency. **(c)** Circuit diagram of the SQUID, terminating the device. **(d)** Close to resonance, the system can be modelled by an LC-oscillator with nonlinear flux-tunable inductance and capacitance.

[1] It turns out that both the effective inductance and capacitance in magnetic flux[51].

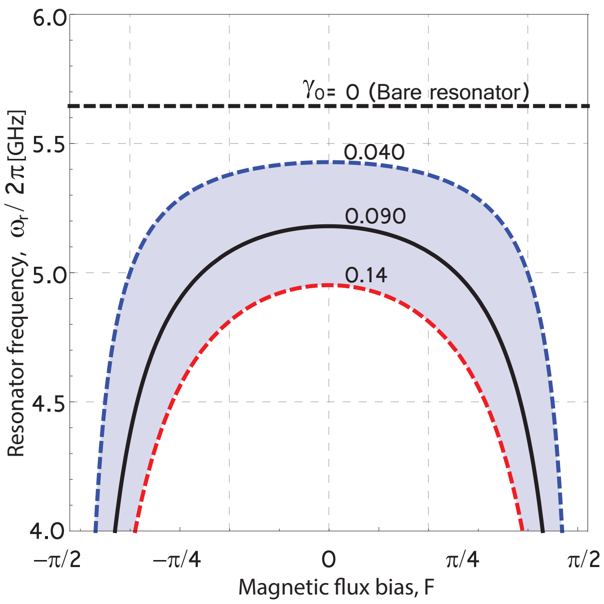

Figure 2.4: The shape of the frequency tuning curve is governed by the inductive participation ratio, γ_0. The black dashed line represents a non-tunable resonator ($\gamma_0 = 0$), whereas the dashed blue, solid black, and dashed red show the tuning curve for $\gamma_0 = 4$, 9, and 14%, respectively.

2.4 The flux-pumped parametric oscillator

The concept of parametric oscillations, first introduced by M. Faraday in 1831[34], is one of the most studied non-linear systems and can be found in many systems ranging from varactor diodes in electrical circuits to swings in the playground. The word "parametric" means that one of the parameters found in the oscillators equations of motion, *e.g.* resonant frequency or damping, is modulated (or pumped) in time at a rate of about twice the oscillator frequency. The consequence of pumping the system parametrically is that oscillations build up, and the amplitude increases exponentially in time until it saturates due to nonlinearities[37]. In contrast to the harmonic oscillator, parametric systems exhibit instabilities which open up possibilities to use these systems as sensitive probes. Although this is a very old field in physics, this phenomenon was first observed in superconducting circuits based on the nonlinear inductance of Josephson junctions by Yurke *et al.* in 1988[35] from which our implementation originates.

In our case, the quarter wavelength tunable resonator can be operated as a parametric oscillator by applying a rf-pump tone with angular frequency $\omega_p \approx 2\omega_r$ to the device in addition to the dc-tuning, see Fig. 2.5(a)[22, 23, 24, 39]. The choice of quarter-wavelength resonator is favorable since it has no mode at the pumping frequency $2\omega_r$, preventing the pump from populating the resonator at the pump frequency. Before the field starts to build up, however, the strength of the pump needs to compensate for the damping of the system. We refer to this point as the *parametric threshold*, separating two operation regimes which will be under discussion throughout this section. In the next section, we follow the formalism and analysis by C. M. Wilson *et al.* [40], based on quantum network theory developed by Yurke and denker[41]. After that, we make the connection to the field amplitude formalism used in Appended paper I, developed by Wustmann and Shumeiko[50][2]. Finally, we introduce a linearized impedance model developed by Sundqvist *et al.*[51] called "the pumpistor".

2.4.1 Parametric amplification below the threshold

Before treating the parametric oscillations, some techniques and intuition can be deployed from first considering the simpler case of small pump amplitude. In this regime below the parametric threshold, we can operate the system as a *parametric amplifier*, in which small probe signals at the resonator frequency can be amplified[23]. In this section, we outline how the gain of the amplifier is calculated by formulating and solving the differential equation describing the dynamics of the system. We consider the case of degenerate parametric pumping ($\omega_p = 2\omega_r$), which leads to phase sensitive parametric amplification. For this case, no additional noise is added to the signal, as oppose to the non-degenerate (phase insensitive) case where half a quantum of noise is added to the amplified signal.

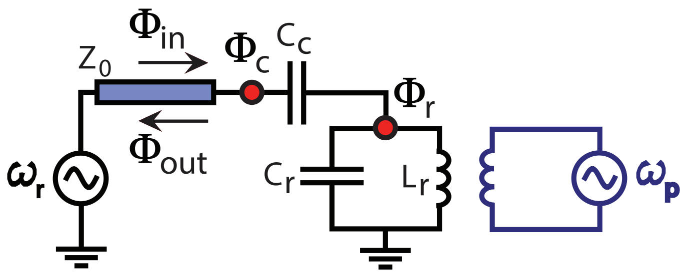

Figure 2.5: The circuit diagram for the flux-pumped parametric oscillator. The canonical flux nodes outside the coupling capacitor and inside the resonator are denoted Φ_c and Φ_r, respectively. The microwave pump (in blue) is inductively coupled to the SQUID of the resonator.

Formulation of the differential equation

The system can be treated in terms quantum network theory and circuit quantization [41, 42], by denoting the canonical flux of each node $\Phi_i = \int_{-\infty}^{t} V_i dt'$, with V_i being the node voltage with reference to ground, see Fig. 2.5(b). The notion is then to consider the scattering of the incoming field, $\Phi_{\rm in}(x,t)$, where x is the position along the line (with the resonator located at $x = 0$). Since the dynamics experimentally is observed by probing the outgoing field $\Phi_{\rm out}(x,t)$, the aim is to relate this field with the incoming one. The solution takes the form of a one-dimensional wave

[2] In these two theoretical descriptions, the normalization convention of the pump amplitude differ. In the quantum network framework, we introduce the dimensionless parameter ϵ'', whereas the field amplitude formalism uses ϵ' with unit of angular frequency.

equation due to the small dimensions of the coplanar waveguide center conductor and gaps

$$\Phi_{\mathrm{c}}(x,t) = \Phi_{\mathrm{in}}\left(\frac{x}{v_{\mathrm{ph}}} + t\right) + \Phi_{\mathrm{out}}\left(-\frac{x}{v_{\mathrm{ph}}} + t\right), \tag{2.9}$$

where the phase velocity $v_{\mathrm{ph}} = 1/\sqrt{LC}$ denote the speed of light in the line. The boundary condition can be derived by taking the space and time derivatives of Eq. (2.9)

$$-\frac{1}{L}\frac{\partial \Phi_c}{\partial x}\bigg|_{x=0} = \frac{1}{Z_0}\left(\frac{\partial \Phi_c}{\partial t} - 2\frac{\partial \Phi_{\mathrm{in}}}{\partial t}\right)\bigg|_{x=0}. \tag{2.10}$$

Then, recalling that the current through an inductor and capacitor can be written $I_{\mathrm{L}} = \frac{\Delta\Phi}{L}$ and $I_{\mathrm{C}} = C\frac{d^2(\Delta\Phi)}{dt^2}$, respectively, where $\Delta\Phi$ is the difference in flux across the element. For node c, Kirchoff's laws yields

$$C_c\left(\frac{d^2\Phi_c}{dt^2} - \frac{d^2\Phi_r}{dt^2}\right) = -\frac{1}{Z_0}\frac{d\Phi_c}{dt} + \frac{2}{Z_0}\frac{d\Phi_{\mathrm{in}}}{dt}, \tag{2.11}$$

whereas, considering node r yields

$$C_c\left(\frac{d^2\Phi_r}{dt^2} - \frac{d^2\Phi_c}{dt^2}\right) = -C_r\frac{d^2\Phi_r}{dt^2} - \frac{1}{L_r}\Phi_r. \tag{2.12}$$

Now, rearranging the terms and divide both sides with $C_c + C_r$ gives

$$\frac{d^2\Phi_r}{dt^2} + \frac{1}{L_r(C_c + C_\kappa)}\Phi_r = \frac{C_c}{C_c + C_r}\frac{d^2\Phi_c}{dt^2}. \tag{2.13}$$

Expressing the resonant frequency as $\omega_r = 1/\sqrt{L_r(C_c + C_r)}$, and the coupling parameter as $\kappa = C_c/(C_c + C_r)$, Eq. (2.13) can be written as

$$\frac{d^2\Phi_r}{dt^2} + \omega_r^2\Phi_r = \kappa\frac{d^2\Phi_c}{dt^2}. \tag{2.14}$$

We include the parametric pumping at angular frequency ω_p and strength ϵ, to arrive at the final differential equation for the system below the threshold. Assuming that the coupling remains constant, the equation takes the form

$$\frac{d^2\Phi_r}{dt^2} + \left(\omega_r^2 + \epsilon\cos(\omega_p t + \phi)\right)\Phi_r = \kappa\frac{d^2\Phi_c}{dt^2} \tag{2.15}$$

Solving the differential equation

Due to the non-linear nature of Eq. (2.15), it cannot be solved using standard techniques from Fourier analysis. Instead, the principles of harmonic balance, also known as slow variables[43], can be used. Consider the following *ansatz* for the canonical flux, where we separate the two quadratures

$$\Phi_i = q_{i,1}\cos\left(\frac{\omega_p}{2}t\right) - q_{i,2}\sin\left(\frac{\omega_p}{2}t\right), \tag{2.16}$$

where $i \in \{c, r\}$ for the quadrature indices. Due to the complex nature of the output, the quadratures are better represented in the complex plane by reformulating the *ansatz* (2.16) as

$$\Phi_i = \frac{u_i}{2}\exp\left(i\frac{\omega_p}{2}t\right) + \frac{u_i^*}{2}\exp\left(-i\frac{\omega_p}{2}t\right), \tag{2.17}$$

where $u_i = q_{i,1} + iq_{i,2}$. Inserting the *ansatz* (2.17) into equation (2.15) gives two differential equations

$$\begin{cases} -C_c\left(\frac{\omega_p}{2}\right)^2(u_c - u_r) = -\frac{i}{Z_0}\frac{\omega_p}{2}u_c + \frac{2}{Z_0}\frac{\omega_p}{2}u_{\text{in}}^0 \\ \left(\omega_r^2 - \left(\frac{\omega_p}{2}\right)^2\right)u_r + \frac{\epsilon}{2}u_r^*\exp(i\phi) = -\kappa\left(\frac{\omega_p}{2}\right)^2 u_c \end{cases}, \tag{2.18}$$

where u_{in}^0 denotes the complex quadrature at the input of the resonator. Now, let us recall the boundary condition in Eq. (2.10) and express it in terms of impedances

$$u_{\text{out}} = \frac{Z_0}{Z_L + Z_0}u_r + \frac{Z_L - Z_0}{Z_L + Z_0}u_{\text{in}}^0 \tag{2.19}$$

Approximate solution

To analytically solve this problem is hard. Therefore, we find an approximate solution by assuming that $Z_L \gg Z_0$ at resonance. We define

$$\kappa Q = \frac{|Z_L(\omega_r)|}{Z_0} = \frac{1}{Z_0 C_c \omega_r} \qquad Q = \frac{C_c + C_r}{Z_0 C_c^2 \omega_r}. \tag{2.20}$$

In the limit when $\kappa Q \gg 1$, we find the lowest order of the solution for the gain

$$g = \frac{q_{\text{out},1} + iq_{\text{out},2}}{\Phi_{\text{in}}^0} = 1 - 2\frac{1 + \epsilon'' \sin(\phi) - i\left(\epsilon'' \cos(\phi) - \delta'\right)}{1 + \delta'^2 - \epsilon''^2}, \tag{2.21}$$

where $\delta' = \left(\frac{\omega_p}{2} - \omega_r\right)/\Gamma = \delta/\Gamma$ and $\epsilon'' = \epsilon Q/(\omega_r\omega_p) = \epsilon/2\Gamma\omega_p$ are the normalized detuning and pump strength, respectively. In Fig. 2.6, the absolute value of the gain expression in Eq. (2.21) for the degenerate parametric amplifier ($\delta' = 0$) is plotted as function of the phase angle between the signal and the pump for three different values of the normalized pump strength, ϵ''. The zero-gain level represents the amount of power needed to compensate for the depth of the reflected magnitude response of the resonator and is thus minimized when the resonator is highly overcoupled, recall Fig. 2.2.

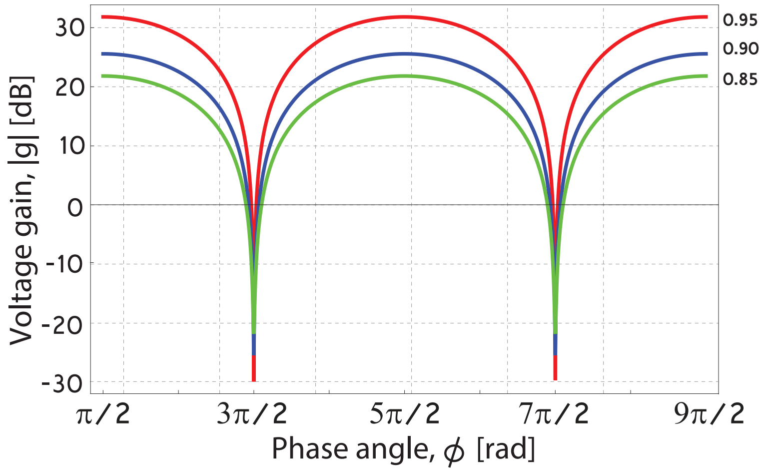

Figure 2.6: Voltage gain curves for the degenerate parametric amplifier as a function of the phase angle between the signal and the pump, ϕ for three different normalized pump strengths below the threshold. $\epsilon'' = 0.95$, 0.90, and 0.85 in red, blue, and green solid lines, respectively. The zero-gain line in black will depend on the magnitude dip of the resonator and can be interpreted as the output power with the parametric pump turned off.

2.4.2 Parametric oscillations above the threshold

The central phenomenon in this thesis takes place when the pump amplitude exceeds the damping ($\epsilon'' > 1$), where the system starts to build up a field inside the resonator, known as parametric oscillations. These occur only within a certain region in the space spanned by the pump-strength, ϵ'' and the pump-resonator detuning, $\delta' = (\omega_p/2 - \omega_r)/\Gamma$. In this section, the conditions needed to build up parametric oscillations are described.

To capture the dynamics of this regime, we need to add the lowest order (cubic) nonlinearity to the equations of motion, taking the form of a Duffing oscillator as described by Dykman[44]

$$\frac{\partial^2 \varphi}{\partial t^2} + 2\Gamma \frac{\partial \varphi}{\partial t} + \left[\omega_r^2 + \epsilon \cos(\omega_p t)\right] \varphi - \alpha \varphi^3 = \xi(t), \tag{2.22}$$

where $\varphi = 2\pi\Phi_r/\Phi_0$, ϵ is the amplitude of the frequency modulation, $2\Gamma = \omega_r/Q$ is the resonance line width corresponding to the damping of the system, and α is the so-called Duffing term describing the dominant nonlinearity of the system. In our system, this term is negative having the mechanical analogue of a softening spring. Finally, $\xi(t)$ on the right hand side of Eq. (2.22) represents the mean-zero noise that induces activated switching between two meta-stable states of the system.

Solution to the differential equation

Similar to the case of solving the equation of motion below the threshold, we need to make certain approximations to find analytical solutions to Eq. (2.22). Again, to solve this class of weakly nonlinear oscillators, we deploy the technique of slow variables[43] where the in-phase and quadrature amplitudes are allowed to vary slowly in time by introducing a slow-time scale, τ, yielding

$$\tau = \Gamma t, \qquad \frac{d}{dt} = \Gamma \frac{d}{d\tau}. \tag{2.23}$$

The method is then to let the "constants" of the *ansatz* be functions of this slow time scale

$$\begin{aligned}\varphi &= q_1(\tau)\cos\left(\frac{\omega_p}{2}t\right) - q_2(\tau)\sin\left(\frac{\omega_p}{2}t\right) = \\ &= \frac{u(\tau)}{2}\exp\left(i\frac{\omega_p}{2}t\right) + \frac{u^*(\tau)}{2}\exp\left(-i\frac{\omega_p}{2}t\right).\end{aligned} \tag{2.24}$$

Now, by assuming small damping ($\Gamma \ll \omega_p \epsilon''$) and neglecting second derivatives due to the slow variables, the first and second derivatives of Eq. (2.24) can be approximated as

$$\frac{d\varphi}{dt} \approx i\frac{\omega_p}{4}\left(u(\tau)\exp\left(i\frac{\omega_p}{2}t\right) - c.c.\right), \tag{2.25}$$

$$\frac{d^2\varphi}{dt^2} \approx -\left(\frac{\omega_p}{2}\right)^2 + i\Gamma\frac{\omega_p}{2}\left(\frac{du}{d\tau}\exp\left(i\frac{\omega_p}{2}t\right) - c.c.\right). \tag{2.26}$$

Moreover, the pump- and cubic nonlinearity terms are approximated by neglecting fast rotating terms

$$\varphi\cos(\omega_p t) \approx \frac{1}{4}\left(u(\tau)\exp\left(-i\frac{\omega_p}{2}t\right) + c.c.\right) \tag{2.27}$$

$$\varphi^3 \approx \frac{3}{8}\left(u|u|^2\exp\left(i\frac{\omega_p}{2}t\right) + c.c.\right) \tag{2.28}$$

Inserting the *ansatz* along with the approximated terms (2.27) and (2.28) into the Duffing equation (2.22), we can express the equations of motion for the system as two coupled differential equations for the in-phase, q_1, and quadrature, q_2, signals

$$\begin{cases} \frac{dq_1}{d\tau} = -q_1 + (\epsilon'' + \delta')q_2 + \alpha'(q_1^2 + q_2^2)q_2 \equiv -q_1 + \frac{\partial g}{\partial q_2} \\ \frac{dq_2}{d\tau} = -q_2 + (\epsilon'' - \delta')q_1 - \alpha'(q_1^2 + q_2^2)q_1 \equiv -q_2 + \frac{\partial g}{\partial q_1} \end{cases}, \tag{2.29}$$

where $\delta' = (\omega_p/2 - \omega_r)/\Gamma = \delta/\Gamma$ is the normalized angular frequency detuning between the pump and the resonator, $\epsilon'' = \epsilon/2\Gamma\omega_p$ is the normalized pump amplitude, and $\alpha' = 3\alpha/4\Gamma\omega_p$ is the normalized Duffing nonlinearity parameter. The function $g = g(q_1, q_2)$ on the right hand side of the two equations in (2.29) is the Hamiltonian of the system describing the meta-potential landscape of the system. This function will be the topic of the next section.

The meta-potential

An intuitive picture for the slow dynamics of the two coupled equations of motion (2.29) can be gained by studying the meta-potential in the rotating frame

$$g(q_1, q_2) = \frac{\delta'}{2}(q_1^2 + q_2^2) + \frac{\epsilon''}{2}(q_2^2 - q_1^2) + \frac{\alpha'}{4}(q_1^2 + q_2^2)^2, \tag{2.30}$$

where the dynamics mimics that of a fictitious particle moving in this meta-potential with two meta-stable states[38]. When no probe signal is sent to the resonator, the two states oscillate with the same amplitude, but are separated in phase by π-radians, see Fig. 2.7. From Eq. (2.30), we see that its shape is governed by the three normalized parameters δ', ϵ'', and α', see Fig. 2.7.

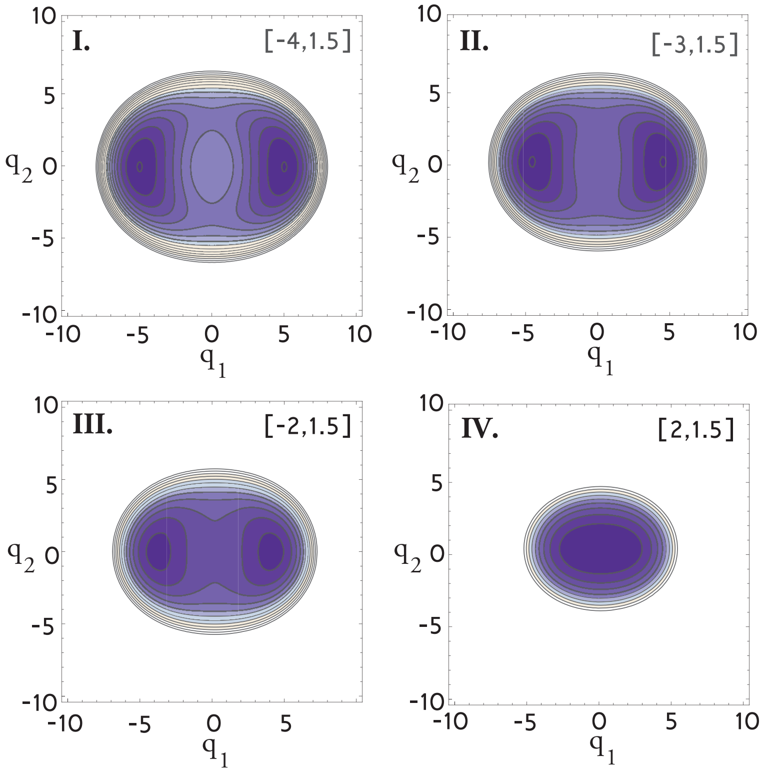

Figure 2.7: Contour plot of the in-phase (q_1) and quadrature (q_2) components of the metapotential in Eq. (2.30) for four different operation points in the plane spanned by the normalized pump-resonator detuning δ' and pump strength ϵ''. The operation points are marked in the upper right corner of each panel and in the plane later in Fig. 2.8.

2.4.3 Region of parametric oscillations

At this point, we know that the parametric oscillations only occur when the pump amplitude is above the threshold ($\epsilon'' > 1$). In addition, the pump frequency needs to be close to degeneracy ($\omega_p \approx 2\omega_r$). In this section we will systematically derive the stability conditions for the parametric oscillations to map out the parametric region in the plane spanned by δ' and ϵ''.

Steady state solutions

The stability conditions (or bifurcation points) of the system can be derived from the equations of motion (2.29), by finding their steady state response

$$\begin{cases} 0 = q_1 - \left(\epsilon'' + \delta' + \alpha' \left(q_1^2 + q_2^2\right)\right) q_2 \\ 0 = q_2 - \left(\epsilon'' - \delta' - \alpha' \left(q_1^2 + q_2^2\right)\right) q_1 \end{cases} . \tag{2.31}$$

The slow variables, q_1 and q_2 are first converted to magnitude, q, and phase, θ, for the oscillations using the following substitution

$$\left[q_1 = \sqrt{\alpha'} q \cos(\theta), \quad q_2 = \sqrt{\alpha'} q \sin(\theta)\right], \tag{2.32}$$

The trivial solution $q = 0$ is omitted by dividing both equations in (2.31) with $\sqrt{\alpha'}q$

$$\begin{cases} 0 = \cos(\theta) - \left(\epsilon'' + \delta' + \alpha' q^2\right) \sin(\theta) \\ 0 = \sin(\theta) - \left(\epsilon'' - \delta' - \alpha' q^2\right) \cos(\theta) \end{cases} \tag{2.33}$$

If we solve for zero amplitude $q = 0$, we find the following solutions

$$q = \sqrt{\pm \frac{1}{\alpha'} \left(\sqrt{\epsilon''^2 - 1} - \delta'\right)}, \tag{2.34}$$

By instead putting the amplitude to zero and solving for the normalized drive strength ϵ'', the symmetric bifurcation curve in Fig. 2.8 is obtained

$$\epsilon'' = \sqrt{\delta'^2 + 1} \tag{2.35}$$

Higher order terms

The region in Eq. (2.35) yields a completely symmetric region which, however, does not agree well with experiments due to the fact that our frequency modulation is affected by the cosine nonlinearity of Eq. (2.8), see Fig. 2.4. Therefore, we need to extend the model to take into account also higher order terms of the mixing product of the pumped flux in the SQUID, see Appended paper II. This *pump-induced nonlinearity* manifests itself as a frequency shift of the region increasing with pump amplitude, see Appended paper I, which we quantify by introducing a dimensionless parameter β, defined as

$$\frac{\omega_r(\epsilon) - \omega_r(0)}{\Gamma} = -\beta\epsilon''^2, \tag{2.36}$$

which gives an extended Duffing equation

$$\frac{\partial^2 \varphi}{\partial t^2} + 2\Gamma \frac{\partial \varphi}{\partial t} + \left[\omega_r^2 + \epsilon \cos\left(\omega_p t\right) - \frac{\beta \epsilon^2}{4\Gamma\omega_p} \left(1 - \cos(2\omega_p t)\right)\right] \varphi$$

$$-\alpha\left[1-\frac{3\lambda}{4\Gamma\omega_p}\epsilon\cos(\omega_p t)\right]\varphi^3=0, \tag{2.37}$$

where we have introduced λ for representing the correction to the Duffing nonlinearity due to the fact that α is modulated by the pump. Again implementing the method of slow variables, we can write down the two coupled differential equations for the equations of motion

$$\begin{cases} \frac{dq_1}{d\tau}+q_1-(\delta'+\epsilon''+\beta\epsilon''^2+\alpha'(q_1^2+(1+\lambda\epsilon'')q_2^2))q_2=0 \\ \frac{dq_2}{d\tau}+q_2+(\delta'-\epsilon''+\beta\epsilon''^2+\alpha'(q_2^2+(1-\lambda\epsilon'')q_1^2))q_1=0 \end{cases} \tag{2.38}$$

After a while, the system reaches steady state and we can reduce these equations to

$$\begin{cases} q_1-(\delta'+\epsilon''+\beta\epsilon''^2+\alpha'(q_1^2+(1+\lambda\epsilon'')q_2^2))q_2=0 \\ q_2+(\delta'-\epsilon''+\beta\epsilon''^2+\alpha'(q_2^2+(1-\lambda\epsilon'')q_1^2))q_1=0 \end{cases} \tag{2.39}$$

Next, let us make the same variable substitution as in Eq. (2.32), and omitting the trivial solution and dropping the next order term of the Duffing nonlinearity $(\lambda=0)$[3], yielding

$$\begin{cases} -\left(\alpha' q^2+\epsilon''+\beta\epsilon''^2+\delta'\right)\sin(\theta)+\cos(\theta)=0 \\ \left(\alpha' q^2-\epsilon''+\beta\epsilon''^2+\delta'\right)\cos(\theta)+\sin(\theta)=0 \end{cases}, \tag{2.40}$$

which can be written as

$$\begin{cases} \cot(\theta)-\alpha' q^2-\epsilon''-\beta\epsilon''^2-\delta'=0 \\ \tan(\theta)+\alpha' q^2-\epsilon''+\beta\epsilon''^2+\delta'=0 \end{cases}. \tag{2.41}$$

From these two equations we can derive the amplitudes and phases corresponding to the stable and unstable solutions

$$q=\sqrt{\pm\frac{1}{\alpha'}\left(\sqrt{\epsilon''^2-1}-\beta\epsilon''^2-\delta'\right)}. \tag{2.42}$$

Similar to the previous case in Eq. (2.35), the amplitude is put to zero and we solve Eq. (2.42) for the normalized drive strength ϵ''. This gives the bifurcation points in Fig. 2.8 defining the parametric region, see Appended paper I,

$$\epsilon''=\frac{\sqrt{1-2\beta\delta'\pm\sqrt{1-4\beta\left(\beta+\delta'\right)}}}{\sqrt{2}\beta}. \tag{2.43}$$

The phase of the parametric oscillations can also be calculated from Eq. (2.41) by instead eliminating the amplitudes, yielding

$$\theta=\arctan\left(\epsilon''\pm\sqrt{\epsilon''^2-1}\right)+n\pi \qquad n\in\{0,1\}, \tag{2.44}$$

where $n=1$ gives the π-shifted states in Fig. 2.7.

[3] We justify this approximation with the argument that the Duffing nonlinearity is not dominant over the pump-induced frequency shift.

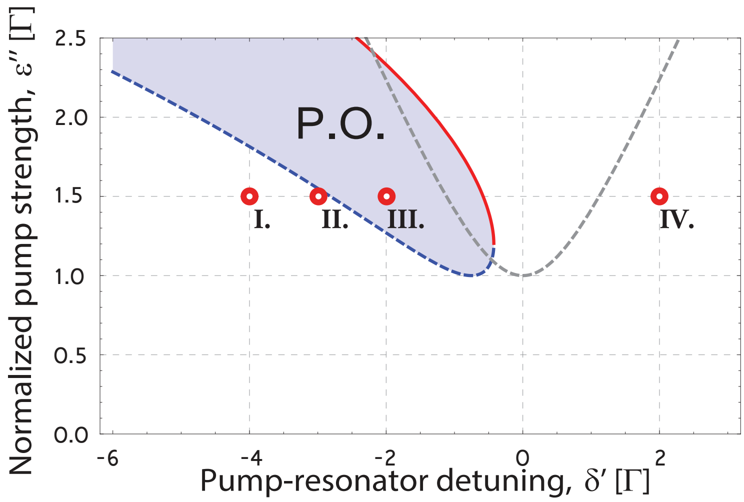

Figure 2.8: Region in which parametric oscillations build up in the resonator in the parameter plane spanned by the effective pump strength and pump-resonator detuning, both normalized to the resonator line width, Γ. The dashed blue line and the solid red line are the solutions to Eq. (2.43) when higher order terms are added to the pump. The dashed gray line is the solution to Eq. (2.35), in absence of higher order pump terms. The four marked points **I-IV** correspond to the four quadrature panels in Fig. 2.7, where the shape of the metapotential is calculated from Eq. (2.30).

2.4.4 Resonator field amplitude formalism

In the previous sections 2.4.1 and 2.4.2, the differential equations for the equations of motion of the system were derived using quantum network formalism for the canonical flux in the resonator. An alternative method, which in some situations is more illustrative, is to consider the field amplitude A inside the resonator, as well as an incoming B and outgoing C flow of photons[50], see Fig. 2.9. This is the method utilized throughout Appended paper I and will here get introduced.

Close to resonance, $\delta \equiv \omega_p/2 - \omega_r \ll \omega_r$, the field amplitude inside the resonator can be treated as a slow variable compared to all other timescales in the system, yielding a simplified Langevin equation for the system dynamics

$$i\dot{A} + \delta A + \epsilon A^* + \alpha |A|^2 A + i\Gamma A = \sqrt{2\Gamma_0} B(t). \tag{2.45}$$

$|A|^2$ gives the number of photons in the resonator, whereas $B(t)$ is the probe field amplitude such that $|B|^2$ has units of photons per second. $\Gamma = \Gamma_0 + \Gamma_R$ is the total damping rate of the system, being the sum of the external, Γ_0, and internal, Γ_R, damping rates. ϵ and α denote the effective pump strength and Duffing parameter, respectively. The full F-dependence of these coefficients can be express in terms of resonator parameters as[50]

$$\epsilon \approx \frac{\delta f \omega_{\lambda/4} \gamma_0}{2} \frac{\sin(F)}{\cos^2(F)} \tag{2.46}$$

$$\alpha \approx \frac{\pi^2 \omega_{\lambda/4} Z_0}{R_K} \left(\frac{\gamma_0}{\cos(F)}\right)^3 = \alpha_0 \left(\frac{\gamma_0}{\cos(F)}\right)^3, \tag{2.47}$$

where $\delta f = \pi \Phi_1/\Phi_0$ is the ac-flux amplitude, $Z_0 = 50\ \Omega$ is the resonator's characteristic impedance, $R_K = h/e^2$ is the quantum resistance, and $\alpha_0 = \pi^2 \omega_{\lambda/4} Z_0 / R_K$.

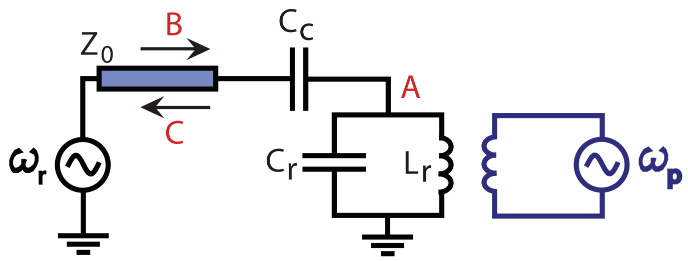

Figure 2.9: In the field amplitude formalism used by Wustmann and Shumeiko[50], the number of photons in the resonator is denoted A, whereas the incoming and outgoing flow are denoted B and C, respectively.

2.5 The "Pumpistor" model

An alternative and more applied way to think about the parametric phenomena in the flux-pumped parametric resonator was developed by K. Sundqvist *et al.*, see Appended paper II. In his model, the SQUID is described as the previously introduced Josephson inductance, see section 1.2.2, in parallel with another element which arises due to the flux pumping. This impedance was named "the pumpistor" and it depends on the phase angle between the probe signal and the pump. In particular, this classical treatment explains the phase response of the degenerate parametric amplifier and can be used as a practical tool when analyzing more complicated parametrically driven circuits. In this section, we give a brief introduction to the theoretical framework of the model. For a more elaborate description, the reader is referred to the Appended paper II.

2.5.1 Expansion of the mixing product

The fundamental concept behind the model is the frequency mixing product of the current flowing through the Josephson junctions, *i.e.* the flux pumped critical current of the SQUID (flux term) and the phase across the two parallel Josephson junctions (phase term), recall Eq. (1.7)

$$I = I_c \left|\cos\left(\pi\Phi_{\mathrm{p}}(t)/\Phi_0\right)\right| \sin(\varphi(t)), \tag{2.48}$$

where the flux of the pump can be written in terms of the dc-flux bias and a small ac-contribution from the pump at angular frequency ω_p with phase θ_p,

$$\Phi_{\mathrm{p}}(t) = \Phi_{\mathrm{dc}} + \Phi_{\mathrm{ac}}\cos(\omega_p t + \theta_p). \tag{2.49}$$

The two terms of Eq. (2.48) are then series expanded separately before they are multiplied together to find an approximation of the circuit impedance. By substituting Eq. (2.49) into the flux term of Eq. (2.48), we series expand around the dc-flux point, Φ_{dc}, yielding

$$I_c \cos\left(\pi\Phi_{\mathrm{p}}(t)/\Phi_0\right) \approx I_c\cos(F) - I_c\sin(F)\delta f\cos(\omega_p t + \theta_p), \tag{2.50}$$

with $F = \pi\Phi_{\mathrm{dc}}/\Phi_0$ and $\delta f = \pi\Phi_{\mathrm{ac}}/\Phi_0$ denoting the normalized dc and ac flux quantities, respectively. Moreover, assuming that the Josephson phase takes the form $\varphi(t) = \varphi_s\cos(\omega_s t + \theta_s)$, this term is expanded using a Fourier-Bessel series

$$\sin(\varphi(t)) = \sum_{n=-\infty}^{\infty} J_n(\varphi_s)\sin\left[n\left(\omega_s t + \theta_s + \frac{\pi}{2}\right)\right], \tag{2.51}$$

where J_n is the $\mathrm{n^{th}}$-order Bessel function of the first kind. The product is calculated, retaining only terms at the signal frequency and neglecting other mixing products. We then define an electrical input impedance at the signal frequency as

$$Z_{\mathrm{SQ}} = i\omega_s L_{\mathrm{SQ}}, \tag{2.52}$$

where the SQUID inductance can be expressed as the Josephson inductance in parallel with the pumpistor inductance[4] $L_{\mathrm{SQ}}^{-1} = L_{\mathrm{J}}^{-1} + L_{\mathrm{P}}^{-1}$, given as

[4]The pumpistor is denoted as an inductor because its impedance is proportional to $i\omega_s$.

$$L_{\mathrm{J}} = \frac{L_{\mathrm{J0}}}{\cos(F)} \left[\frac{\varphi_s}{2J_1(\varphi_s)} \right] \approx \frac{L_{\mathrm{J0}}}{\cos(F)}, \tag{2.53}$$

$$L_{\mathrm{P}} = \frac{-2\mathrm{e}^{i\Delta\theta}}{\delta f} \frac{L_{\mathrm{J0}}}{\sin(F)} \left[\frac{\varphi_s}{2J_1(\varphi_s) - 2\mathrm{e}^{i2\Delta\theta} J_3(\varphi_s)} \right] \approx -\frac{L_{\mathrm{J0}}}{\sin(F)} \frac{\mathrm{e}^{i\Delta\theta}}{\delta f}, \tag{2.54}$$

with $L_{\mathrm{J0}} = \hbar/(2eI_c)$ and $\Delta\theta = 2\theta_s - \theta_p$. Thus, the SQUID can be represented as the equivalent circuit in Fig. 2.10(a), with the Josephson inductance in parallel with the pumpistor as an alternative formalism to the nonlinear differential equations presented in section 2.4. Next, we will investigate the phase angular dependence of the pumpistor and how to interpret it in terms of gain of a parametric amplifier.

2.5.2 Phase angle and negative resistance

An important property of the inductance of the pumpistor in Eq. (2.54) is that it is dependent on the phase angle $\Delta\theta$ between the signal and pump, which makes it responsible for the phase sensitivity of the degenerate parametric amplifier when $\omega_p = 2\omega_r$. When studying the behavior of the pumpistor, we note that the phase angle puts the device in four different regimes, illustrated in Fig. 2.10(b). When $\Delta\theta = 0$ or π, the pumpistor acts as a negative or positive inductance contribution to the Josephson inductance. However, at $\Delta\theta = \pi/2$, it acts as a resistor which leads to additional attenuation or de-amplification in the device. Finally, when the pumpistor reaches $\Delta\theta = -\pi/2$, it acts like a negative resistor, which provides gain by injecting energy from the pump. Another way to formulate the negative resistance is in terms of a negative internal quality factor, $Q_i < 0$. For the implementation of a degenerate parametric amplifier, this imposes some guidelines of operation regime for the amplifier. Maximum squeezing (and thus amplification), occurs when the system is close to (but below) its parametric bifurcation threshold. In terms of quality factors, this gives the condition that $(-Q_e < Q_i < 0)$. Using the linearized impedance of the SQUID, also the gain of the amplifier can be calculated and related to the phase angle, see [51].

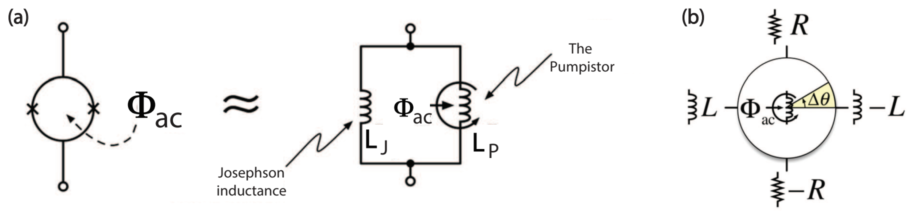

Figure 2.10: **(a)** The equivalent circuit of the SQUID as a Josephson inductance in parallel with the pumpistor. **(b)** The impedance of the pumpistor is govern by the phase angle $\Delta\theta = 2\theta_s - \theta_p$. When $\Delta\theta = -\pi/2$, it acts like a negative resistor where the pump injects energy into the resonator, providing gain.

2.6 The transmon superconducting qubit

2.6.1 The Cooper-Pair Box

Today, there are several flavors of superconducting qubits, including charge, phase, and flux qubits (and combinations thereof). The names refer to the respective quantum mechanical degree of freedom, utilized to encode the states of the qubit. One of the most commonly used is the transmon qubit[25], a combination of a charge and a phase qubit derived from the Cooper-pair box (CPB) charge qubit[26, 27, 28]. To understand the physics of the transmon, it is therefore pedagogic to start out from the CPB.

The CPB consists of a small aluminum island, connected to a superconducting reservoir through a Josephson junction on one side and biased by a gate capacitance C_g and a gate voltage V_g on the other side, see Fig. 2.11(a). When the junction is in its superconducting state, Cooper pairs can tunnel to- and from the island. The potential of the island can be controlled through the gate voltage.

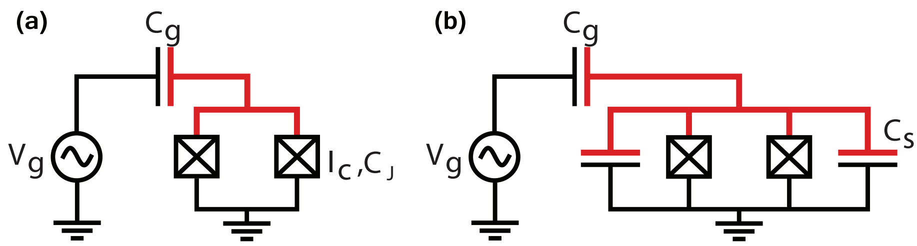

Figure 2.11: (a) The circuit diagram of the Cooper Pair Box. The island (in red) is biased with a gate voltage V_g through a gate capacitance C_g and separated from the reservoir by two parallel Josephson junctions of critical current I_c and junction capacitance C_J. **(b)** The corresponding circuit diagram for the transmon qubit, in which two shunt capacitors, C_s have been introduced to reduce the charging energy, E_C.

The system is characterized by two energies; the *Josephson energy*, E_J is the accumulated potential energy in the junctions as a super current passes through it, given as

$$E_\mathrm{J} = \frac{\Phi_0 I_c}{2\pi} = \frac{R_Q \Delta}{2R_n}, \tag{2.55}$$

where $R_\mathrm{Q} = \frac{h}{4e^2}$ and R_n are the quantum and normal state resistances, respectively. Δ is the superconducting energy gap related to the critical temperature of the material[5]. Whereas the *charging energy* is the (generalized) kinetic energy needed to transfer one electron across the capacitor

$$E_\mathrm{C} = \frac{e^2}{2C_\Sigma}, \tag{2.56}$$

[5]The critical temperature for bulk aluminum is $T_\mathrm{c} = 1.176$ K [29]. However, the effective T_c for a thin film is slightly higher than for bulk material ≈ 1.4K. According to BCS theory [8], $\Delta = 1.76 k_\mathrm{B} T_\mathrm{c}$.

where $C_\Sigma = C_\mathrm{g} + C_\mathrm{J}$ represents the total capacitance between the island and its circuit environment. In addition the system is characterized by the reduced gate charge $n_g = C_g V_g/2e$. In most practical implementations of qubits, it is convenient to be able to tune its transition frequency. This is obtained in the same way as for the tunable resonator in Sec. 2.3, by adding another Josephson junction is in parallel with the first one, forming a dc-SQUID with flux-tunable Josephson energy, $E_\mathrm{J} \to E_\mathrm{J}(\Phi_\mathrm{dc})$. The effective Josephson energy is then given as

$$E_\mathrm{J}(\Phi_\mathrm{dc}) = E_\mathrm{J}^\mathrm{max} \left|\cos\left(\frac{\pi\Phi_\mathrm{dc}}{\Phi_0}\right)\right|, \tag{2.57}$$

where $\Phi_0 = h/2e$ is the flux quantum. For further information about the SQUID the reader is referred to textbooks such as [31]. The Hamiltonian of the CPB can now be written in terms of these two energies in the charge basis

$$\hat{H}_\mathrm{CPB} = 4E_\mathrm{C} \sum_{n=-\infty}^{\infty} (n-n_g)^2 |n\rangle\langle n| - \frac{E_\mathrm{J}}{2} \sum_{n=-\infty}^{\infty} \left[|n+1\rangle\langle n| + |n\rangle\langle n+1|\right]. \tag{2.58}$$

By doing the transformation $n \to -i\frac{d}{d\phi}$ the Hamiltonian in Eq. (2.58) takes the form of a quantum rotor in phase space

$$\hat{H}_\mathrm{CPB} = 4E_\mathrm{C}(-i\frac{d}{d\phi} - n_g)^2 - E_\mathrm{J}\cos\phi. \tag{2.59}$$

The exact solutions to the Hamiltonian in Eq. (2.59) are obtained using Mathieu functions [25], plotted in Fig. 2.12. In order to operate the system as a qubit, it is essential that it can be considered a two-level system, *i.e.* the two lowest eigenenergies must be well-separated from any higher energy levels of the system. In Fig. 2.12(a) the charge dispersion relations for the three lowest eigenenergies are plotted as a function of the reduced gate charge n_g and $E_\mathrm{J}/E_\mathrm{C}$. The bands form a periodic structure where the energy required for transitions between the ground state $|0\rangle$ and the first excited state $|1\rangle$ is smallest when the gate charge $n_g = m + \frac{1}{2}$, for integer numbers of m. The CPB is thus mainly characterized by the energy ratio $E_\mathrm{J}/E_\mathrm{C}$. The two limiting regimes where $E_\mathrm{J}/E_\mathrm{C} \ll 1$ and $E_\mathrm{J}/E_\mathrm{C} \gg 1$ are referred to the *charge*- and *phase* limits, respectively, shown in Fig. 2.12 (b) and 2.12(c). However, even though the goal of obtaining an effective two-level system is fulfilled, the CPB has one major drawback in its dependence of keeping the charge constant at the sweet spot. Due to the environment, the qubit will be subject to fluctuations of the gate charge, known as charge noise. This means that the level spacing between the two levels will fluctuate and lead to short quantum coherence times. In 2002, Vion *et al.* [30] demonstrated that these half-integer values of the reduced gate charge (so called *sweet spots*) serve as optimal working points for operating the qubit.

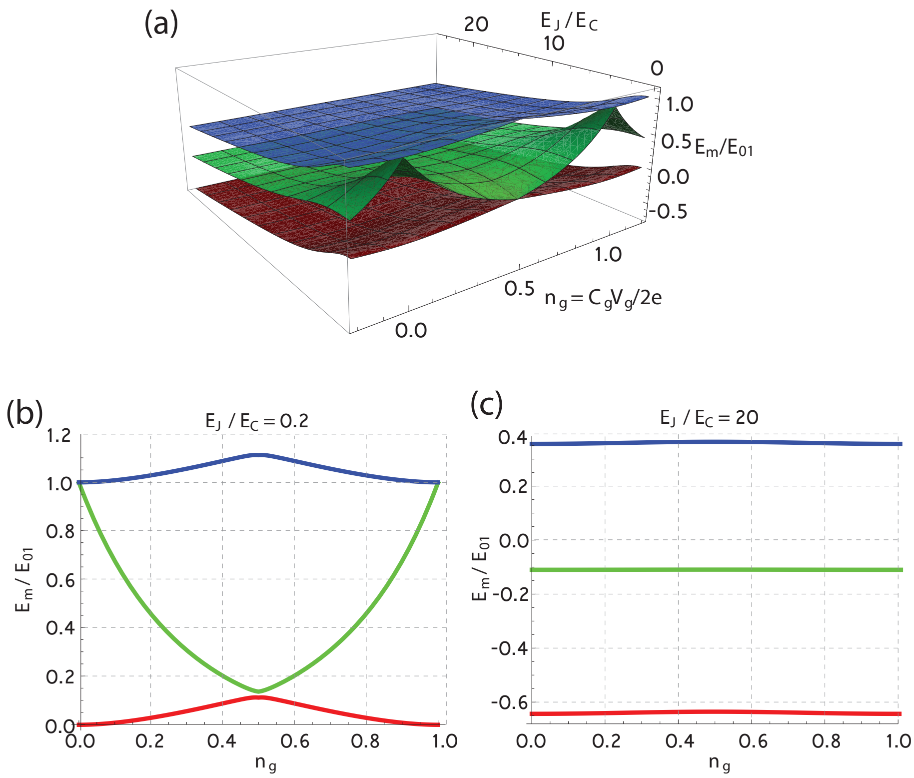

Figure 2.12: a) Calculated energy band diagram for the three lowest energy levels as a function of reduced gate charge and ratio of E_J/E_C. **(b)** The charge limit diagram when $E_J/E_C = 0.2$ for the CPB. **(c)** The phase limit or transmon regime, plotted for the case when $E_J/E_C = 20$.

2.6.2 The transmon regime

To overcome the sensitivity to charge noise of the CPB, the transmon qubit was proposed by Koch *et al.* [25] and is today one of the most popular qubit designs. As compared with its ancestor, the charging energy of the transmon is reduced. This is obtained by increasing the sizes of the two islands, see Fig. 2.11(b), thus introducing a dominant capacitance in parallel with the two Josephson junctions, recall the expression in Eq. (2.56). This has the consequence that $E_{\mathrm{J}}/E_{\mathrm{C}}$ is taken away from the charge limit and instead entering a new regime, known as the transmon regime. The frequency needed to drive transitions between the transmon's ground state $|0\rangle$ and first excited state $|1\rangle$, can be well approximated as

$$\omega_a/\hbar \approx \sqrt{8E_{\mathrm{J}}E_{\mathrm{C}}} - E_{\mathrm{C}}. \tag{2.60}$$

Two essential quantities need to be introduced in the energy band diagram in Fig. 2.12(a), namely the charge dispersion and the relative anharmonicity. The charge dispersion is defined as $\epsilon_m = E_m(n_g = \frac{1}{2}) - E_m(n_g = 0)$, *i.e.* the peak-to-peak value of the variation of eigenenergy of the m^{th} level. The smaller the charge dispersion gets, the less the qubit frequency will change in response to gate charge fluctuations. Thus, the charge dispersion is a measure of the qubit's sensitivity to charge noise.

The relative anharmonicity is defined as the level spacing between the energy levels of the system and is given as $\alpha_r = (E_{12} - E_{01})/E_{01}$, where E_{01} and E_{12} are the energy level spacings of the system. Too small anharmonicity leads to the risk of driving unwanted higher transitions if too strong pulses are used. Thus, the transmon no longer act as a qubit but rather a multi-level system. Both the charge dispersion and the anharmonicity has a common dependence in the ratio of the Josephson and the Coulomb energies $E_{\mathrm{J}}/E_{\mathrm{C}}$. As Koch *et al.* derived, the charge dispersion decreases exponentially when $E_{\mathrm{J}}/E_{\mathrm{C}}$ is increased and becomes almost flat when $E_{\mathrm{J}}/E_{\mathrm{C}} \gtrsim 20$. However, the prize to pay for the reduced charge dispersion is that the anharmonicity of the energy levels also decreases. Fortunately, the latter has only a weak power dependence on $E_{\mathrm{J}}/E_{\mathrm{C}}$. Thus, it is possible to enter into a regime where the transmon is virtually insensitive to charge noise, maintaining a sufficiently large anharmonicity for the system to act as an effective two-level system. This range of $E_{\mathrm{J}}/E_{\mathrm{C}} \gtrsim 20$ for which the transmon has sweet spots everywhere is known as the transmon regime, see Fig. 2.12(c). The transmon can also be regarded as an unbiased phase qubit.

2.6.3 Dispersive readout of qubits

The interaction between the quantized field inside the resonator with frequency ω_r and the two-level artificial atom with transition frequency ω_a can be described by the Jaynes-Cummings model[32, 33]. In this model, the resonator is described by the Hamiltonian of a harmonic oscillator in terms of the creation and annihilation operators, $\hat{a}^\dagger$ and $\hat{a}$, respectively. If we only allow the qubit (or atom) to be in two states, we use the Pauli z-matrix notation for a spin-1/2 system, $\hat{\sigma}_z = \hat{\sigma}_{00} - \hat{\sigma}_{11} = |0\rangle\langle 0| - |1\rangle\langle 1|$. The Hamiltonian of the coupled system is given as

$$\hat{H} = \hbar\omega_r \left(\hat{a}^\dagger\hat{a} + \frac{1}{2}\right) + \frac{\hbar\omega_a}{2}\hat{\sigma}_z + \hbar g\left(\hat{\sigma}_+ + \hat{\sigma}_-\right)\left(\hat{a} + \hat{a}^\dagger\right), \tag{2.61}$$

where $\hat{\sigma}_+ = \hat{\sigma}_{01} = |0\rangle\langle 1|$ and $\hat{\sigma}_- = \hat{\sigma}_{10} = |1\rangle\langle 0|$ describes the processes of de-exciting and exciting the atom, respectively. The last term of the Hamiltonian in Eq. (2.61) denotes the interaction between the atom and the resonator and consists of four terms. Two of these, $\hat{\sigma}_-\hat{a}^\dagger$ and $\hat{\sigma}_+\hat{a}$, share the property of conserving energy since the excitation is moved between the two systems. The two other terms, *i.e.* $\sigma_+\hat{a}^\dagger$ and $\sigma_-\hat{a}$ can be dropped when the coupling rate is much smaller than the transition frequencies, $g \ll \omega_a, \omega_r$. This operation is known as the rotating wave approximation and yields the common form of the Jaynes-Cummings Hamiltonian, representing an important tool when analyzing system dynamics in most quantum optics experiments

$$\hat{H}_{\mathrm{JC}} = \hbar\omega_r \left(\hat{a}^\dagger\hat{a} + \frac{1}{2}\right) + \frac{\hbar\omega_a}{2}\hat{\sigma}_z + \hbar g\left(\hat{\sigma}_+\hat{a} + \hat{\sigma}_-\hat{a}^\dagger\right). \tag{2.62}$$

Within the framework of the Jaynes-Cummings model, there are two very distinct regimes which we will describe next.

The resonant regime of vacuum Rabi oscillations

When the resonator and atom are close to resonance with each other ($\omega_r \approx \omega_a$), the photon number state of the resonator, $\hat{n} = \hat{a}^\dagger\hat{a}$, and the two states $|0\rangle$ and $|1\rangle$ of the qubit are no longer eigenstates of the Hamiltonian in Eq.(2.62). Instead, the system takes eigenstates on the form of entangled states between the resonator and qubit states

$$|n, \pm\rangle = \frac{|0\rangle\,|n\rangle \pm |1\rangle\,|n-1\rangle}{\sqrt{2}}, \tag{2.63}$$

where the splitting between the symmetric and anti-symmetric superposition states are split by $\sqrt{n}2g\hbar$. At the point when the two systems are exactly on resonance, $\omega_r = \omega_a$, energy will get coherently swapped between the two systems at a rate $\Omega_R = \sqrt{n}g/\pi$, known as the vacuum Rabi frequency. By measuring the size of the avoided level crossing, the coupling rate g can be experimentally extracted.

The dispersive regime of cavity pull and ac-Stark shift

The next important regime is when the atom and resonator are far detuned from each other, such that $\Delta = |\omega_a - \omega_r| \gg g$, no atomic transitions can exchange photons between the systems. However, fortunately for quantum information technology, there is still a dispersive coupling present, which gives rise to small frequency shifts. In this so-called *dispersive regime*, the Hamiltonian can no longer be solved analytically. Instead, by using second order time dependent perturbation theory in terms of g/Δ, it can be approximated by

$$\hat{H}_{\mathrm{DISP}} = \hbar\left(\omega_r + \frac{g^2}{\Delta}\hat{\sigma}_z\right)\left(\hat{a}^\dagger\hat{a} + \frac{1}{2}\right) + \frac{\hbar\omega_a}{2}\hat{\sigma}_z, \tag{2.64}$$

where the resonator frequency has picked up a term which is dependent on the state of the atom, $\tilde{\omega}_r = \omega_r \pm g^2/\Delta$. This shift allow us to perform *dispersive read-out* by projecting the qubit state onto $|0\rangle$ or $|1\rangle$, without decohering the state (since no photon is needed for the process).

Another way to analyze the dispersive Hamiltonian in Eq. (2.64) is obtained by re-arranging the terms, moving the shift to the atomic transition frequency, such that

$$\hat{H}_{\mathrm{DISP}} = \hbar\omega_r \left(\hat{a}^\dagger\hat{a} + \frac{1}{2}\right) + \frac{\hbar}{2}\left(\omega_a + \frac{2g^2}{\Delta}\hat{a}^\dagger\hat{a} + \frac{g^2}{\Delta}\right)\hat{\sigma}_z. \tag{2.65}$$

Now, instead of letting the qubit pull the resonator, we see that the photon number in the resonator, $\hat{n}$ give rise to a shift of the qubit transition frequency by an amount of $2g^2/\Delta$ per photon, known as the *ac-Stark shift*. In addition, it is shifted by a constant frequency of g^2/Δ. This shift originates from the zero-point energy of the resonator and is known as the *Lamb shift*.

Chapter 3

Experiments

3.1 Device modeling

3.1.1 Bare resonator design

The starting point when designing a parametric quarter wavelength resonator is to match its characteristic impedance to the outside world, ($Z_c = Z_0 = 50\ \Omega$). As we recall from section 1.3, the characteristic impedance of the transmission line is governed by the inductance and capacitance per unit length through the relation $Z_c = \sqrt{L/C}$. Thus, to match impedances, we need to simulate L and C for a given dielectric environment of the planar structure using conformal mapping techniques[46] in a Mathematica script based on the tailored equations resembling the cross-sectional geometry of our device, in Fig. 3.1(a), see Appendix C. The implemented model can be used for both single and bilayer substrates. In our case, the silicon wafer with relative dielectric constant of $\epsilon_1 = 11.68$ and thickness $h_1 = 380\mu$m, is coated with $h_2 = 400$ nm of wet grown oxide with $\epsilon_2 = 3.9$. In Table 3.1, the geometrical input parameters are presented, whereas the generated output parameters, illustrated in Fig. 3.1(b), are presented in Table 3.2.

w	g	h_1	h_2	h_3	h_4	ϵ_1	ϵ_2
10.00	5.500	380.0	0.400	380.4	500.0	11.68	3.900

Table 3.1: Input dimension parameters for the conformal mapping script, all length dimensions are given in units of μm.

ϵ_{eff}	v_{ph} [ms^{-1}]	C [pFm^{-1}]	L [μHm^{-1}]	l [μm]
6.34	0.397×c	165	0.426	4960

Table 3.2: Output parameters from the conformal mapping script.

After establishing the cross sectional design, the acquired knowledge about the effective dielectric constant can be used to calculate the fundamental frequency mode of the resonator using Eq. (2.1) for a certain physical length l

$$f_{\lambda/4} = \frac{c}{4l\sqrt{\epsilon_{\mathrm{eff}}}}, \tag{3.1}$$

3.1.2 Coupling capacitor

The next important design aspect for the resonator is to engineer its coupling to the microwave probe line, which is set by the coupling capacitor, C_c. Often, it is convenient to design the coupling capacitor having in mind the external quality factor (and consequently the external damping rate, Γ_0) which refers to the loss rate of photons through the capacitor. The external quality factor can be related to the coupling capacitor using the lumped element representation of the resonator connected to a load impedance Z_0 as

$$\begin{aligned} Q_{\mathrm{e}} &= \frac{(1+(\omega_{\lambda/4}C_cZ_0)^2)(Cl/2+C_c)}{\omega_{\lambda/4}C_c^2Z_0} \approx \\ &\approx \frac{Cl/2+C_c}{\omega_{\lambda/4}C_c^2Z_0} = \frac{\sqrt{L_r/C_c}}{Z_0}\left(1+\frac{Cl/2}{C_c}\right)^{3/2}, \end{aligned} \tag{3.2}$$

where the bare angular frequency of the resonator is given as

$$\omega_{\lambda/4} = 1/\sqrt{L_r(Cl/2+C_c)}. \tag{3.3}$$

Eq. (3.2) thus allows us to calculate the coupling capacitance needed to obtain a certain external quality factor. For instance, if we aim for an external quality factor of $\mathrm{Q_e} = 5000$, this corresponds to a coupling capacitance of $C_c = 4.9$ fF for a bare resonator frequency $\omega_{\lambda/4} = 2\pi \times 5.5$ GHz.

The next, and perhaps more challenging question to address is what physical design of capacitor will result in the desired capacitance for our dielectric environment at hand. We calculate the capacitance of the interdigital finger capacitor using an electromagnetic simulator in MicroWave Office. A micrograph of a coupling capacitor and the four-port simulation setup are illustrated in Fig. 3.1(b), with resulting output parameters.

3.1.3 Non-linear SQUID inductance

After the bare resonator has been designed, we turn our attention to the non-linear contribution to its total inductance, dictating its frequency tunability as well as parametric properties. From section 1.2.2, we recall that the Josephson inductance is governed by the critical current of the two parallel junctions according to the relation

$$L_s = \frac{\Phi_0}{2\pi I_c\left|\cos(\pi\Phi_{\mathrm{dc}}/\Phi_0)\right|}. \tag{3.4}$$

From the theory section of the parametric oscillator in section 2.4, we know that the dynamics of the device is governed by the amount of nonlinearity present in the system. Since the nonlinearity originates from the Josephson inductance we can choose its involvement by designing the participation ratio of Josephson inductance to geometrical inductance of the coplanar waveguide, given as

$$\gamma_0 = \frac{L_{\mathrm{s},0}}{Ll} \qquad L_{\mathrm{s},0}\,\big|_{\Phi_{\mathrm{dc}}=0} = \frac{\Phi_0}{2\pi I_c}. \tag{3.5}$$

Therefore, we recall the outcome of the inductance per unit length from the conformal mapping model in Fig. 3.1(b), which tells us the total geometrical inductance of the resonator, $L_r = Ll$ and provides guidance when choosing Josephson inductance given that we aim for a certain value of γ_0. Experimentally, a reliable estimate of the Josephson inductance can be obtained by measuring the normal state resistance of identically fabricated test structures, placed within four-point measurement sites on-chip, see Fig. 3.1(c). From the measured normal state resistance, R_n, the Josephson inductance can be calculated as

$$L_{\mathrm{s},0} = \frac{\Phi_0 R_n}{\pi^2 \Delta}, \tag{3.6}$$

where $\Delta \approx 0.2$ meV denotes the superconducting gap of Al. As we will discuss in the next section, the Josephson junctions are fabricated by oxidizing the Al during the two-angle evaporation sequence. It is intuitive that a longer oxidation time and higher pressure will generate a thicker insulating barrier between the two superconducting Al electrodes. Therefore, the tuning of Josephson inductance can in part be done during the clean room processing by tuning the two-angle evaporation and oxidation parameters after a certain design has been exposed in the e-beam lithography.

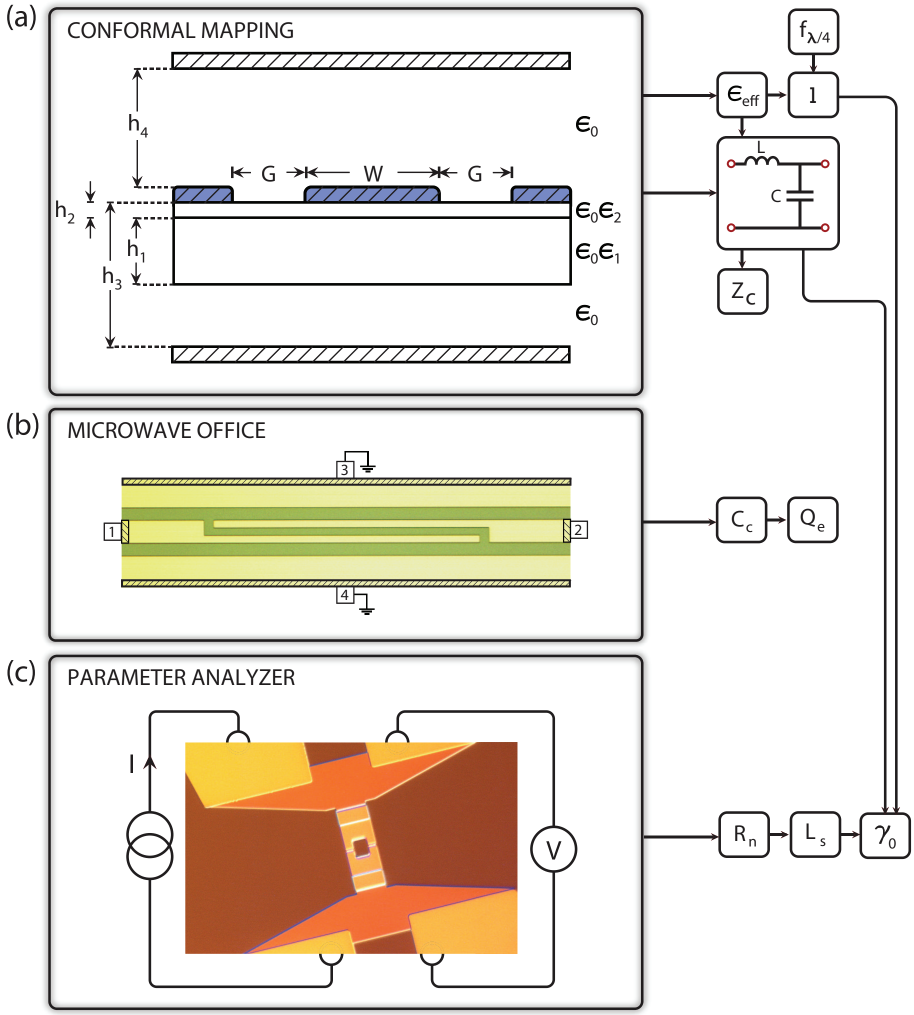

Figure 3.1: Overview of the modeling and design processes. **(a)** Cross section dimensions of the coplanar waveguide geometry. The thicknesses of each layer are denoted h_1-h_4 to the left. The superconducting metal (in dashed blue), is placed on top of a bilayer substrate with dielectric constants ε_1 and ε_2, and is surrounded by top and bottom enclosures separated by vacuum from the device. The output parameters are the inductance and capacitance per unit length as well as the effective dielectric constant from which the characteristic impedance can be calculated. **(b)** Micrograph illustrating how the capacitance of the interdigital finger capacitor is extracted using a four-port electromagnetic simulation in MicroWave Office. The output parameter of the simulation is the coupling capacitance, which via Eq. (3.2) gives us the external quality factor.**(c)** Micrograph of one of the four-point resistance test structure sites on the samples. A current is injected between the left most pads, whereas the voltage across the junction is measured on the other side, allowing for cancellation of the probe resistance. The output parameter is the normal state resistance, leading to the Josephson inductance through Eq. (3.6). Finally, using Eq. 3.5, the participation ratio, γ_0 can be calculated.

3.2 Fabrication

To fabricate devices containing features on the nano-scale requires a delicate mixture of science and art. The scientific aspect of the work tells us that it needs to be carried out within a clean and well controlled environment, whereas the art lies in the fact that passion as well as experience are key ingredients in any successful clean room process. All fabrication was done in the Nanofabrication Laboratory at Chalmers University of Technology. Throughout this section, we will introduce the main clean room techniques used for fabricating the parametric resonators on 3" p-doped silicon wafers with 400 nm of wet grown oxide. For the detailed recipe, the reader is referred to Appendix A.

3.2.1 Photolithography

Due to the large variations in feature dimensions and resolution requirements, processing time can be saved by first using photolithography to define the large features, *e.g.* contact pads and ground planes. The main steps in this process are described in Fig. 3.2(a)-(e). After cleaning the wafer, it is coated with a lift-off resist (LOR3B) and a positive photoresist (S1813)[1], see Fig. 3.2(a). Using a mask aligner, the coated wafer is then exposed to UV-light through a soda-lime photomask, see Fig. 3.2(b). To develop the exposed pattern, the wafer is immersed into a water-based solvent (MF319), which dissolves the exposed resist, while leaving the parts covered by the mask. The top resist acquires edges with high resolution, whereas the bottom resist has the property of forming an undercut, see Fig. 3.2(c). After the development, organic residues from the resists are etched away in oxygen plasma before the wafer is placed in an electron-beam evaporator with high vacuum. For contact pads, a trilayer metal stack is evaporated. First, 3 nm thin layer of Ti is deposited as a sticking layer to improve the SiO_2/Au adhesion. Then, 80 nm of Au is evaporated as contact material, followed by 10 nm of Pd acting as a stopping layer to prevent diffusion between the Au and Al, see Fig. 3.2(d). Finally, the excess metal is lifted-off using S1165 Remover, dissolving all remaining resist, see Fig. 3.2(e).

3.2.2 Electron beam lithography

Due to the limited resolution of photolithography, as well as our need for design flexibility, a JEOL JBX-9300FS electron beam lithography machine is used to define the resonators as well as Josephson junctions. This process is described in Fig. 3.2(f)-(h). Since we want to evaporate Al, we spin coat the wafer with a bilayer resist system of MMA/ZEP, see Fig. 3.2(f). As the name e-beam lithography suggests, the pattern is then directly transferred into the resist by a beam of electrons with an acceleration voltage of 100kV. The dose used for the ZEP on silicon wafer is set to 150 μCcm^{-2}, see Fig. 3.2(g). In order to avoid the so-called proximity effect due to back scattering of electrons from the substrate, the pattern is divided into 16 different doses based on the surroundings to correct for this effect. A script in the software PROXECCO is used to calculate the proximity correction where small

[1]Positive resist refers to the polymer property that the parts exposed by UV-light can be dissolved in solvent during the development.

features are given a higher dose. After the exposure, the top layer is developed selectively in 96% o-xylene, see Fig. 3.2(h). Finally, just prior to the evaporation of Al, the bottom resist is developed using a mixture of isopropanol and deionized water, 1:4. It is here very important to investigate the undercut properly at the point in the design where it is most critical, *i.e.* where the Josephson junctions will be formed.

3.2.3 Two-angle evaporation

After defining the smallest features in the electron beam lithography, the Josephson junctions are created using two-angle evaporation (shadow evaporation) of aluminum[45] in an electron beam evaporator from Plassys. A sequential description of this process is shown in Fig. 3.2(i)-(l). First, a bottom layer of Al is evaporated under an angle η of the stage on which the sample is mounted. Typically, this layer is between 20-50 nm thick. After finishing the first Al layer, the acceleration voltage of the source electrons is ramped down, and the load lock is filled with O_2-gas at a PID-regulated pressure, P_{ox}. This forms a thin insulating barrier of amorphous Al_xO_y, see Fig. 3.2(j). The oxygen is pumped out after a desired oxidation time, t_{ox} has elapsed. To define the top electrode, a second layer of Al is evaporated from the opposite angle, $-\eta$ as compared with the bottom layer, see Fig. 3.2(k). When choosing the thickness of the top electrode, it is essential to keep in mind which thicknesses the evaporated film need to have step coverage to. In this case, this layer needs to be thicker than the first layer. In addition, since we also use Ti/Au/Pd contacts, the total Al thickness needs to exceed that of the contact layers. Finally, the resist is lifted off, and we are left with the Josephson junctions, see Fig. 3.2(l). In addition to the design dimensions of the two tunnel junctions, its critical current can be tuned using the two oxidation parameters, t_{ox} and P_{ox}.

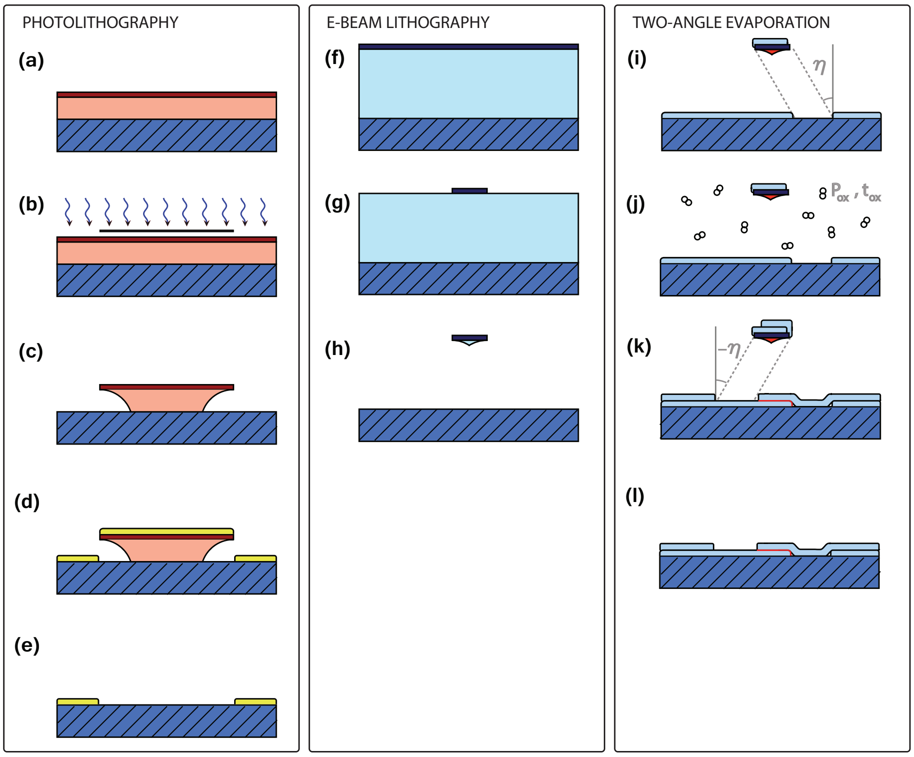

Figure 3.2: The main steps of the fabrication processes. **(a)-(e)** describes the photolithography process used to define and deposit the contact metals for bond pads, ground planes, and test structures. In **(f)-(h)**, the electron beam lithography process is used to define the Josephson junctions, as well as the superconducting resonator. Finally, the junctions are evaporated using two-angle evaporation, shown in **(i)-(l)**.

3.3 Cryogenic measurements

Measurements involving superconducting devices rely on our ability to create a low noise environment for the samples by cooling them far below the critical temperature of the superconducting materials $T \ll T_c$. Therefore, we perform the measurements in a ^{4}He/^{3}He cryogen-free dilution refrigerator with a base temperature of 15 mK. The cooling mechanism is based on a phase separation that occurs when a mixture of ^{4}He and ^{3}He is cooled down to low temperatures (T<0.86K), giving rise to two different concentration phases of ^{3}He, since this isotope is the lighter one a ^{3}He rich phase (concentrated phase) collects on top of the ^{4}He-rich phase (diluted phase). The cooling takes place when the ^{3}He is transported from the concentrated phase to the diluted phase through a phase boundary. This process takes place inside the mixing chamber (M/C) and is the coolest part of the cryostat. However, before this cooling effect can happen, we need to be able to condense the helium, which can be done in a few different ways depending on the type of cryostat. The measurements contained in this thesis were done in three different cryostats. At Chalmers, an Oxford 400 HA wet dilution refrigerator was used, where a 1K pot is used to condense the mixture in the system. At MIT and Queensland cryogen-free dilution cryostats from Leiden and Bluefors were used where there is no need for a bath of ^{4}He to pre-cool the system. Instead, a compressor is used to pump on a pulse tube, transferring ^{3}He gas back and forth inside the core of the cryostat, cooling the system down to 3K.

3.3.1 Measurement setup

Prior to the cryogenic characterization, the samples were mounted in a home-made sample box. The box consists of four parts, each computer numerical control (CNC) milled out from oxygen-free copper. In order to improve thermal anchoring as well as electrical conductivity, a few micron of gold was electroplated on each part, see Appendix A.2. Next, the box is connectorized with SMA connectors and fed through the box walls using glass beads. Inside the box, microstrip launchers are threaded onto the glass beads and soldered on the center conductor of a printed circuit board (PCB) made from Rogers RO3010 with an effective dielectric constant of $\epsilon_r \approx 10$, matching the effective dielectric constant of silicon and sapphire at cryogenic temperatures. The sample is glued into a milled hole in the PCB to get thermal anchoring from the box on the backside and align the edge of the sample with the top of the circuit board. The sample is then bonded to the PCB using gold wire of diameter 25 μm. It is important to fit as many bonds as possible in order to improve the microwave transmission and reduce the inductance of the wire. The device is then mounted on the M/C tail of the cryostat.

To characterize the samples, a microwave setup was installed in the cryostat, see Fig. 3.3. Several aspects need to be taken into account when wiring up the cryostat. First, due to the limited cooling power of the fridge, the cables and components need to be well thermally anchored at each temperature stage not to heat up the system. The coaxial cables are therefore chosen to have poor thermal conductivity between the higher temperature stages while still not attenuating very much, see Fig. 3.3. At the lower temperatures, however, superconducting coax-lines are used with the properties of low attenuation but still with poor thermal conductivity. Since the cryostat cooling power is very different at the various stages, attenuators are attached to the lines, thermalizing their inner conductors. The amount of attenuation is chosen such that the resulting noise temperature matches the stage at which it is mounted.

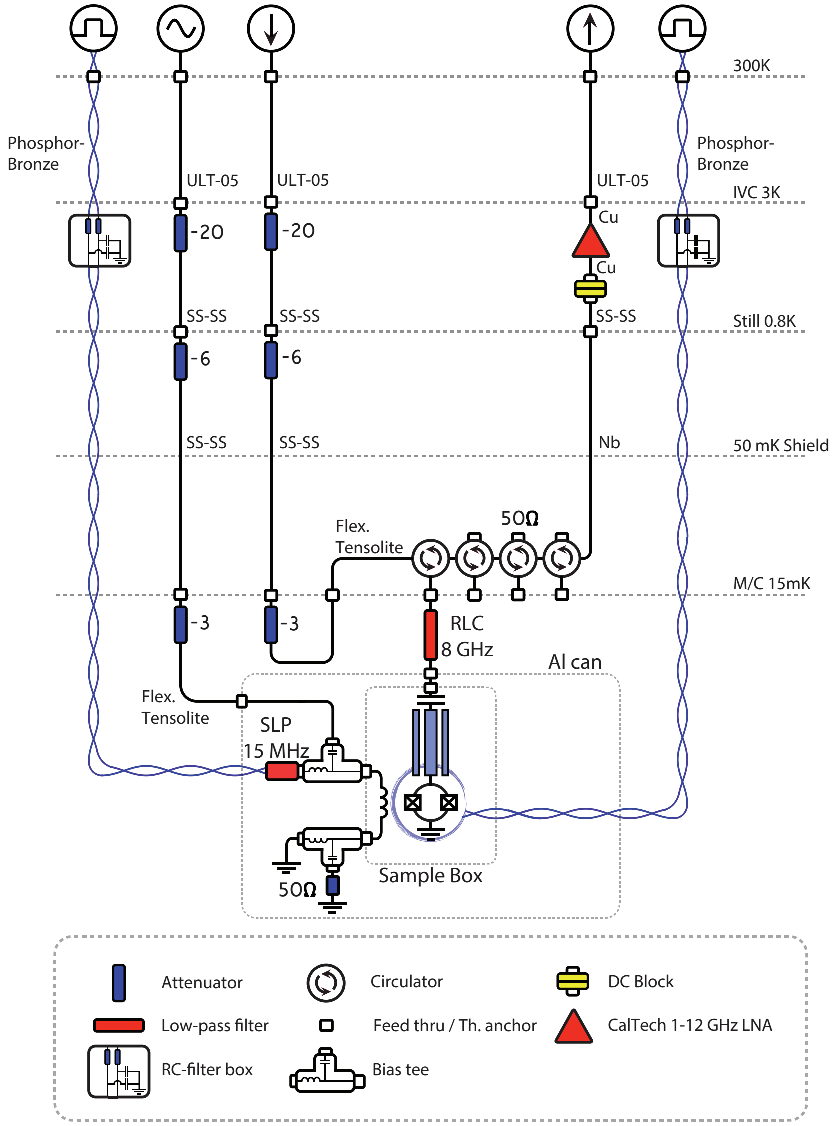

Figure 3.3: Schematic of the cryogenic microwave setup used in the Leiden cryostat at MIT.

Chapter 4

Results

In this chapter, the experimental characterization sequence of a parametric resonator is presented. First, we show how the fundamental behavior of the device can be extracted by studying the line width as well as the frequency tuning curve. By doing a power sweep, we extract the Duffing parameter from the shift in resonant frequency. Second, the probe signal is turned off to suppress the Duffing influence and instead study the parametric oscillations upon modulation of the flux at twice the resonant frequency. From the region of parametric oscillations we extract information about the pump-induced nonlinearity as a consequence of rectification of the frequency tuning curve. Finally, the chapter is concluded by describing the interplay between the two dominant nonlinear effects as a function of magnetic flux bias.

4.1 Static characterization

4.1.1 Frequency tuning curvature

The first important step when characterizing the parametric resonator is to measure its resonance frequency dependence on static dc-flux bias, $F = \pi\Phi_{\mathrm{dc}}/\Phi_0$ using a vector network analyzer. However, since the device exhibits the behavior of a Duffing oscillator, the line shape of the resonator magnitude response as well as its resonant frequency is dependent on the probe power. This effect is more pronounced when the critical current of the Josephson junctions is reduced, *i.e.* when the resonator is far detuned from its maximum frequency $F \rightarrow \pm\pi/2$. In Fig. 4.1(a), the Duffing response is shown and we can find a power level below which the line width is more linear showing a Lorentzian response[1]. This is important when extracting quality factors and damping rates since Eq. (2.5) only is valid for

[1]The traces shown in Fig. 4.1(a) are taken from a device containing transmon qubits and is thus not listed in Table 4.1, due to dispersive shifts of the resonator frequency, see section 2.6.3.

a Lorentzian line shape.

After identifying a power level below which the resonator exhibits linear response, we continue by sweeping the magnetic flux, F, and measure the magnitude and phase of the reflection coefficient, S_{11}. In Fig. 4.1(b), the resonant frequencies for two devices, with slightly different participation ratios γ_0, are extracted for each point in flux and fitted to the function in Eq.(2.8) we recall from section 2.3

$$\omega_r(F) \approx \frac{\omega_{\lambda/4}}{1 + \gamma_0 / |\cos(F)|}. \tag{4.1}$$

Besides the participation ratio, we can also extract the bare resonator frequencies, $\omega_{\lambda/4}$ in absence of the SQUID inductance. The extracted parameters for these two devices are presented in Table 4.1.

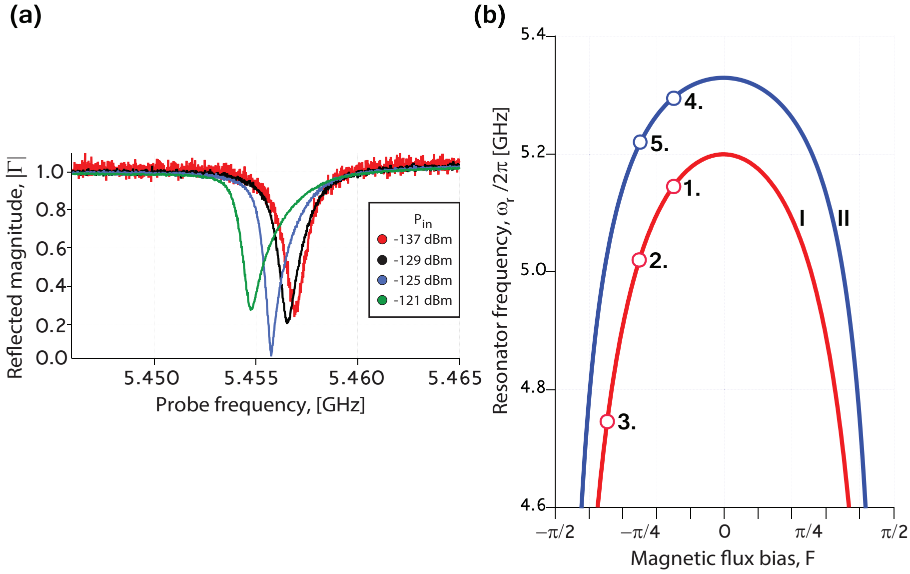

Figure 4.1: (a) The reflected magnitude response for incrementally increase of the probe power for a sample with a more pronounced Duffing nonlinearity. **(b)** Extracted resonant frequencies for the two devices in Table 4.1, fitted to Eq. (4.1), with different inductive participation ratios, γ_0, yielding slightly different frequency-flux curvatures.

Sample	$\omega_{\lambda/4}/2\pi$ [GHz]	$\omega_r(0)/2\pi$ [GHz]	γ_0	I_c [μA]
I	5.645	5.200	0.0898	2.18
II	5.626	5.344	0.0563	3.48

Table 4.1: Extracted resonator parameters for the two measured samples. $\omega_{\lambda/4}$ and $\omega_r(0)$ are the bare- and zero-flux resonant frequencies, respectively. γ_0 denotes the inductive participation ratio and I_c is the critical current of the SQUID.

4.1.2 Duffing nonlinearity

After extracting the participation ratio from the frequency tunability, we investigate the effective Duffing parameter, α which relates to both γ_0 and the magnetic flux bias recalling Eq. (2.47)

$$\alpha \approx \alpha_0 \left(\frac{\gamma_0}{\cos(F)}\right)^3, \tag{4.2}$$

with $\alpha_0 = \pi^2\omega_{\lambda/4}Z_0/R_K$ and $R_K = h/e^2$ being the quantum resistance. We can extract the Duffing parameter by measuring the frequency shift of the resonator by probing it with incrementally increasing powers at a fixed bias point, see Appended paper I, but far below the parametric instability threshold at which the system bifurcates[48, 49], see Fig. 4.2. The resonance undergoes a nonlinear frequency shift from $\delta\omega|_{A=0} = 0$ to $\delta\omega|_{A\neq 0} = -\alpha|A|^2$, where $|A|^2$ is the number of photons in the resonator and α represents the frequency shift per photon. This nonlinear shift can be expressed in terms of the probe power $|B|^2$ (in units of photons per second) and the resonator damping rates,

$$\delta\omega = -\frac{2\alpha\Gamma_0}{\Gamma^2}|B|^2. \tag{4.3}$$

We extract the Duffing parameter α using Eq. (4.3) at three bias points of sample I, see Fig. 4.1, plotted along with the measured reflected phase response in Fig. 4.2 and listed in Table 4.2.

Flux bias	$\omega_r/2\pi$ [GHz]	$\Gamma_0/2\pi$ [kHz]	$\Gamma_R/2\pi$ [kHz]	$\alpha/2\pi$ [kHz/photon]	α/α_0 [$\times 10^{-3}$]
$F_1 = -0.15\pi$	5.1558	429	354	108	0.996
$F_2 = -0.25\pi$	5.0427	344	310	215	1.99
$F_3 = -0.35\pi$	4.7785	482	299	813	7.53

Table 4.2: Extracted parameters from sample I. ω_r is the resonator frequency at the three different flux-bias points. $\Gamma_0 = \omega_r/Q_\mathrm{e}$ and $\Gamma_R = \omega_r/Q_\mathrm{i}$ are the external and internal damping rates, respectively, related to their corresponding quality factors Q_e and Q_i, extracted at low probe power. α represents the Duffing shift per photon.

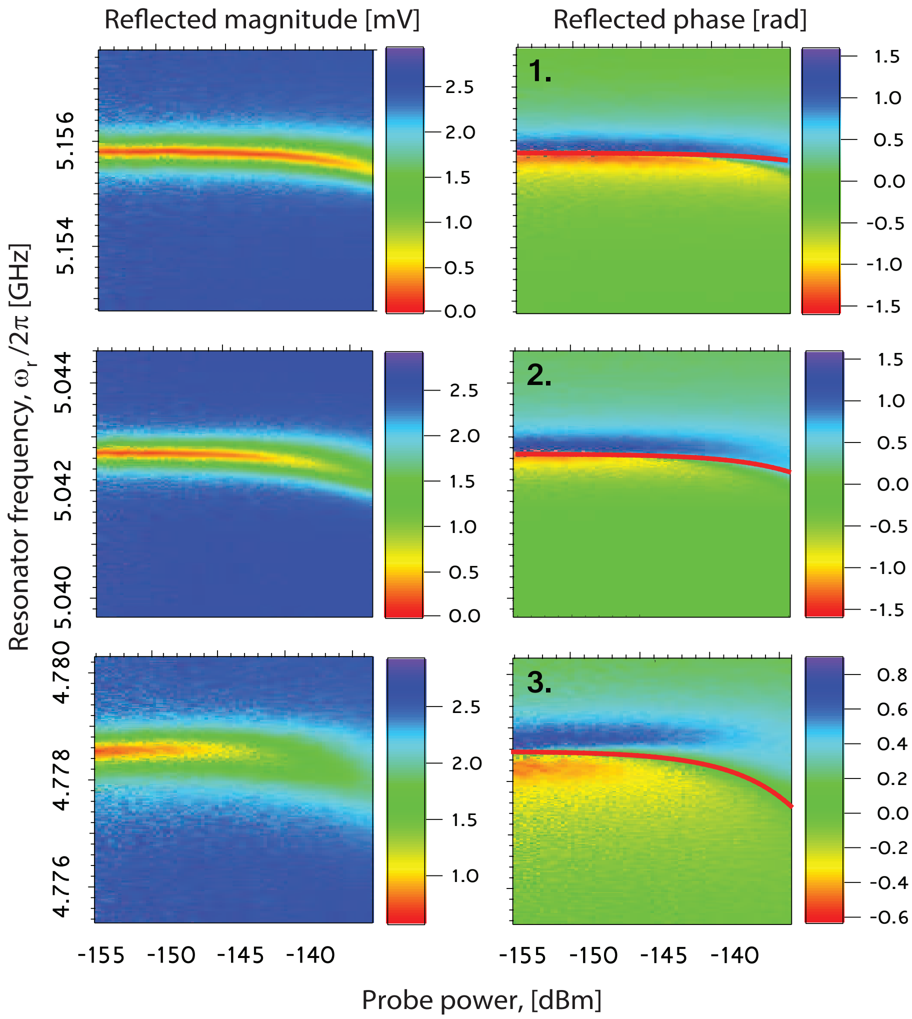

Figure 4.2: Reflected magnitude and phase responses for the three dc flux-bias points for sample I: $F_1 = -0.15\pi$, $F_2 = -0.25\pi$, and $F_3 = -0.35\pi$, in Fig. 4.1(b). The Duffing term gives rise to a nonlinear shift of the resonant frequency as the probe power on the chip is increased. The shift gets more pronounced and affects the resonator at lower probe powers when $F \to \pm\pi/2$, as indicated by the solid red lines in the reflected phase panels, showing a fit to Eq. (4.3) for parameters presented in Table 4.2.

4.2 Parametric characterization

4.2.1 Pump induced nonlinearity

The second nonlinear effect we study enters the dynamics when the parametric pumping is turned on and gets sufficiently strong for higher order terms of the mixing product expansion to affect the resonator[51, 52]. To investigate this nonlinearity, we minimize the Duffing nonlinearity by turning off the probe signal. We then parametrically pump the flux degenerate around a bias point a bit higher up on the flux curve where the Duffing influence is weaker, compare Table 4.2. As we recall from Eq. (2.36), the first higher-order term is proportional to the square of the pump strength and has the effect of shifting the resonator down in frequency as a consequence of rectification in the flux−frequency transfer function. As with the Duffing parameter, the pump-induced nonlinearity parameter can be expressed in terms of γ_0 and F as

$$\beta = \frac{\beta_0}{\gamma_0}\frac{\cos^3(F)}{\sin^2(F)}, \tag{4.4}$$

with $\beta_0 = \Gamma/\omega_{\lambda/4}$. We reveal this effect by detecting the region of parametric instability in the parameter-plane spanned by the pump−resonator detuning δ' and the effective pump strength ϵ', see Fig. 4.3. The energy of the field inside the resonator originates from the pump, and starts to build up exponentially in time when ϵ' is sufficiently strong to compensate for the total damping rate of the resonator: $\epsilon' = \Gamma$. After pumping for some time, the field saturates to a steady state set by the Duffing nonlinearity at the given point in the $(\delta' - \epsilon')$-plane, which we expect to shift the resonator frequency out from the degenerate parametric pumping condition, $\omega_p \approx 2\omega_r$. The boundaries represent the bifurcation threshold at which the resonator enters into the parametric bistable regime, where oscillations in one of two metastable states of the system Hamiltonian occur[38]. In Fig. 4.3, the theoretical prediction from Eq. (2.43) is compared with the experimental observation of the parametric region.

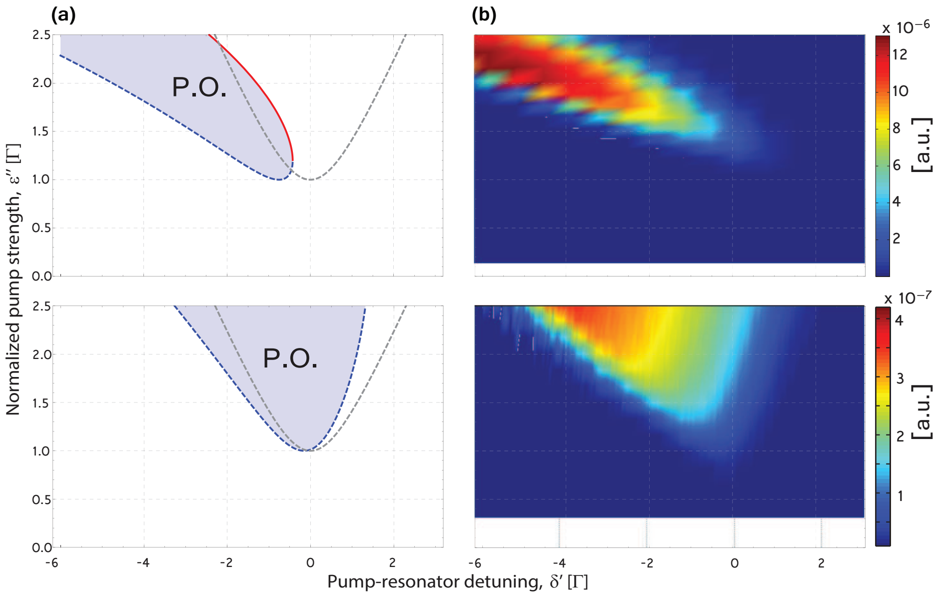

Figure 4.3: **(a)** Theoretical parametric-oscillation region (P.O.) in the $(\delta' - \epsilon')$-plane. The dashed blue and solid red lines are the two solutions to Eq. (2.43), whereas the dashed gray line indicates the symmetric region in Eq. (2.35), in the absence of a pump-induced frequency shift β. The two filled theoretical regions are plotted for $\beta_0 = 0.22$. The top and bottom traces are plotted for magnetic flux bias points $F_4 = -0.15\pi$ and $F_5 = -0.25\pi$, respectively. **(b)** Measured amplitude response around half of the pump frequency at the same bias points as the theoretical curves $F_4 = -0.15\pi$ (top) and $F_5 = -0.25\pi$ (bottom) for sample II, see Fig. 4.1(b). The faces of the data are interpolated to guide the eye.

4.2.2 The metapotential

Now, let us look at a method used to monitor the metapotential of the parametric resonator[38]. By collecting histograms of the in-phase and quadrature voltages, at different operation points in the $[\epsilon', \delta']$-plane, the shape of the metapotential gets reflected, recall section 2.4.2. In Fig. 4.4, collected histograms at four different values of ϵ', δ' are shown. As shown in ref. [38] and explained in the figure caption there can be one, two, or three stable states in the system.

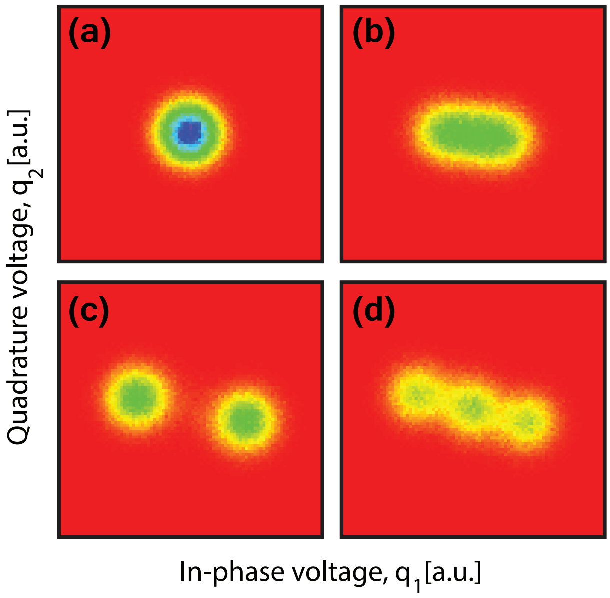

Figure 4.4: Collected histograms of in-phase and quadrature voltage pairs at four different points in the $[\epsilon, \delta]$-plane. **(a)** Outside of the parametric oscillation region the background noise yields the centered gaussian distribution. **(b)** Below the parametric threshold, the distribution get elongated as it starts to get sqeezed in a certain direction set by the pump−signal phase angle. **(c)** Inside the P.O. region, the two meta stable states, separated by π-radians are equally populated. **(d)** Due to the pump-induced nonlinearity, operation points to the left of the degenerate pump frequency, result in co-existence of the "quiet" and "populated" states.

4.3 Interplay between nonlinearities

After studying the Duffing- and pump-induced nonlinearities, there are some important connections to make between the nonlinear effects, magnetic flux bias, and participation ratio, γ_0. In Fig. 4.5(b), the interplay between the two nonlinearities is plotted as a function of the magnetic flux bias, for three different values of γ_0. From the plot, it is clear that the two nonlinear effects contribute differently at different flux bias regimes. When the resonant frequency is close to its maximum, $(F \to 0)$, the Duffing nonlinearity is suppressed, whereas the pump-induced nonlinearity dominates. On the other hand, when the resonator is far detuned from the top, ($F \to \pm\pi/2$), the pump-induced nonlinearity is suppressed and the Duffing nonlinearity dominates.

To summarize we have determined the participation ratio, γ_0 by studying the flux tuning of the resonance frequency. We have extracted the Duffing parameter, α from the power dependent frequency shift of the resonator and we extract the pump nonlinearity β from the other parameters according to Eq. (4.4).

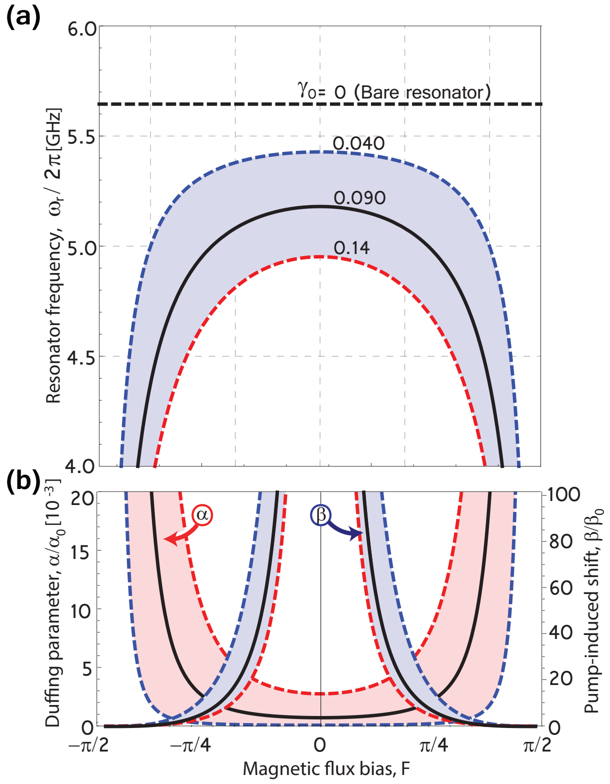

Figure 4.5: **(a)** The resonator frequency as a function of magnetic flux from Eq. (4.1) for a bare non-tunable resonator ($\gamma_0 = 0$) (black dashed line) and three values of the inductive participation ratio $\gamma_0 = 0.040$, 0.090, and 0.14, in dashed blue, solid black, and dashed red, respectively. **(b)** Magnetic-flux dependence of the normalized Duffing nonlinearity parameter, α/α_0 from Eq. (4.2) (left axis) and pump-induced frequency shift parameter, β/β_0 from Eq. (4.4) (right axis), shown in red and blue regions, respectively. The three different traces correspond to the same values of γ_0 as in (a).

Chapter 5

Conclusions & Outlook

In this work we have fabricated and characterized superconducting quarter wavelength resonators with tunable frequency. We have extracted and analyzed two leading nonlinearities in the system. By tuning the resonant frequency of the resonator, we extracted the amount of nonlinearity reflected in the participation ratio. At three different bias points, the Duffing nonlinearity was extracted and analyzed by studying the Duffing response of the resonator line shape as the probe power was gradually increased. Then, the parametric properties of the device was investigated by studying the region of parametric oscillations in the plane spanned by the pump detuning and the pump strength.

The main conclusion from the measurement and analysis is that both nonlinearities originates from the curvatures of the frequency tuning curve, which in turn is governed by the inductive participation ratio of the Josephson inductance, γ_0. The two nonlinear effects originate from different effects and are dominant in different regimes of magnetic flux bias. The Duffing nonlinearity scales with the first derivative of the tuning curve, and is therefore maximum when $F \to \pm\pi/2$, but suppressed for $F \to 0$. The opposite is true for the pump-induced nonlinearity, which is dependent on the second derivative of the tuning curve. This allow us to in-situ tailor both nonlinearities. However, the minimum value of the Duffing parameter $\alpha_0\gamma_0^3$ is set by the participation ratio, but it can be tuned upwards.

The interplay between these nonlinearities also open the possibility to design more complicated devices with desired nonlinear response. One interesting device to realize would be to use the parametric oscillations to encode quantum information by using it as a read-out for a transmon qubit coupled to the center conductor. The read-out would then be based on the dispersive cavity pull that is dependent on the state of the qubit. By operating the parametric resonator close to its parametric region, the dispersive shift can be used to push the system between the oscillating- and quiet states. The signal-to-noise ratio of the parametric oscillations ought to be sufficient to discriminate the ground state from the excited in a single-shot measurement, necessary for quantum information technologies.

Appendix A

Clean room processes

A.1 Recipe for parametric resonators

In this appendix, we present the clean room recipes used for fabricating the parametric resonators. All devices were fabricated on p-doped 3”-silicon wafer with a 400 nm wet grown oxide in the Nanofabrication Laboratory at Chalmers.

1. Cleaning the wafer

1165 Remover	$60-70°$C, 10 min
	Rinse in IPA and blowdry with N_2
Ultrasonic bath	100%, 1 min
IPA bath	Circulation 2 min
QDR bath	Rinse in IPA and blowdry with N_2

2. Photolithography to define alignment marks and bonding pads

Stripping plasma	250 W, 40 sccm O_2, 1 min
Pre-bake on hotplate	110°C, 1 min
Spin lift-off resist LOR3B	3000 rpm, 1 min, $t_{acc} = 1.5$ s ($t \approx 350$nm)
Softbake on hotplate	200°C, 5 min
Spin photoresist S1813	3000 rpm, 1 min, $t_{acc} = 1.5$ s ($t \approx 150$nm)
Softbake on hotplate	110°C, 2 min
Expose pattern	MA6 mask aligner, Lo-vac mode, $P_{vac} = 0.4$ bar
	6 W/cm^2, $t_{exp} = 8.5$
Develop in MF319	45 s (Lift up and rinse after 20 s.)
QDR bath	Rinse in IPA and blowdry with N_2

3. Electron beam evaporation of metals in Lesker PVD225

Ashing in O_2-plasma	50 W, 20 s
E-beam evaporation	$P_{ch} \leq 10^{-7}$mbar
	Sticking layer (Ti), 30Å, 1 Å/s
	Contact layer (Au), 800Å, 1-2 Å/s
	Stopping layer (Pd), 100Å, 1 Å/s
Lift-off in 1165 Remover	$60-70°$C, $t \approx 30$ min
	Rinse in IPA and blowdry with N_2

4. Semi-dicing of wafer from backside	
Spin protective resist S1813	3000 rpm, 1 min, $t_{acc} = 1.5$ s (t $\approx$ 350nm)
Softbake on hotplate	110°C, 3 min
Alignment cuts (frontside)	One cut in each axis for backside alignment
Semi-cuts (backside)	Dice the wafer with sample sized pitches
	Leave $\approx 170\mu m$.
Strip resist in 1165 Remover	$60 - 70$°C, $t \approx 10$ min
	Rinse in IPA and blowdry with N_2 ($\times$ 3 times)

5. Electron beam lithography to define resonators and Josephson junctions	
Ashing in oxygen plasma	50 W, 20 s
Spin lift-off resist MMA(8.5)EL10	500 rpm, $t_{acc} = 2$ s for 5 s
	2000 rpm, $t_{acc} = 5$ s for 45 s ($\approx$ 570 nm)
Softbake on hotplate	170°C, 5 min
Spin e-beam resist ZEP 520A(1:1)	3000 rpm, $t_{acc} = 1.5$ s, 1 min ($\approx$150 nm)
Softbake on hotplate	170°C, 5 min
Expose JEOL JBX-9300FS	100kV, 2nA (70nA) for small (large) features,
	Nominal dose: $150\mu C/cm^2$,
	16 proximity corrected layers.
Cleave wafer	Divide the wafer into rows smaller pieces
Develop top resist	O-xylene, 96%, 2 min
	Dip in IPA and immediately blowdry with N_2

6. Two-angle evaporation of Josephson junctions in Plassys	
Develop bottom resist	H_2O:IPA 1:4, 4 min 50 s (undercut $\geq 0.2\mu$m)
Ashing in oxygen plasma	50 W, 20 s
Electron beam evaporation	$P_{ch} \leq 3 \times 10^{-7}$mbar
Bottom layer of Al	40 nm, 5Å/s, $\alpha = 28°$
Dynamic oxidation	$P_{ox} = 0,2$ mbar, $t_{ox} = 30$ min
Top layer of Al	65 nm, 5Å/s, $\alpha = -28°$
Lift-off in 1165 Remover	$60 - 70$°C, $\approx$20 min
	Rinse in IPA and blowdry with N_2

A.2 Electroplating of gold

Preparations

1. Pour the BDT 200 gold solution in a plastic beaker and heat it up by placing it in heated DI water bath. Set the bath temperature set point to 80°C and monitor the BDT temperature using a stick thermometer. When it has reached 58°C, reduce the set point of the water bath to 60°C.
2. Heat up another glass beaker of water to 55°C on a hotplate. This water is for rinsing the goldplated pieces.
3. Prepare a plastic beaker of copper etch solution.
4. Place the magnet stirrer on the bottom of the beaker and make sure it can rotate freely.
5. Measure the surface area of all the pieces.
6. Stick down the metal grid into the gold solution such that the surface area is the same as the work piece.
7. Mount the workpiece on a metal wire or clamped with tweezers and attach it to the other electrode.

Gold plating procedure

1. Turn on the plating and carefully ramp up the current such that the current density (≈ 2 mA/cm^2) matches the size of the work piece.
2. Monitor the surfaces to ensure that the gold sticks to the work piece. If not, turn off the current and re-mount the work piece. This can also be needed if the gold has not reached all surfaces of the work piece.
3. Let the piece be in the plating bath for about 20 min in total.
4. Ramp down the current and turn off the power supply.
5. Dip the mounted workpiece in the 55° C water beaker and then rinse it with the DI-water gun.
6. Blowdry with N_2.

Appendix B

Resonator fitting function

In order to extract the quality factors of the resonator (driven in its linear regime), we derive an expression for the lumped element representation of the resonant cavity, see Fig. 2.1(b), valid close to resonance. The reflection coefficient, S_{11} can be related to the impedance of the probe line, Z_0 and the resonator, Z_r as[11]

$$S_{11} = \frac{Z_r - Z_0}{Z_r + Z_0} \tag{B.1}$$

where the impedance of the lumped element resonator circuit is

$$Z_r = \frac{1}{i\omega C_c} + \left(\frac{1}{R_r} + \frac{1}{i\omega L_r} + i\omega C_r\right)^{-1} = \frac{1 - \omega^2 L_r(C_r + C_c) + \frac{i\omega L_r}{R_r}}{i\omega C_c(1 - \omega^2 L_r C_r) - \frac{\omega C_c L_r}{R_r}} \tag{B.2}$$

Substitution of (B.2) into (B.1) yields

$$S_{11} = \frac{1 - \omega^2 L_r \left(C_r + C_c\left(1 - \frac{Z_0}{R_r}\right)\right) + i\omega\left(\frac{L_r}{R_r} - Z_0 C_c\left(1 - \omega^2 L_r C_r\right)\right)}{1 - \omega^2 L_r \left(C_r + C_c\left(1 + \frac{Z_0}{R_r}\right)\right) + i\omega\left(\frac{L_r}{R_r} + Z_0 C_c\left(1 - \omega^2 L_r C_r\right)\right)} \tag{B.3}$$

Assuming that $R_r \gg Z_0$ and introducing $\omega_0 = 1/\sqrt{L_r(C_r + C_c)}$ and $x = \omega/\omega_0$ yields

$$S_{11} = \frac{1 - x^2 + ix\omega_0\left(\frac{L_r}{R_r} - Z_0 C_c\left(1 - x^2\omega_0^2 L_r C_r\right)\right)}{1 - x^2 + ix\omega_0\left(\frac{L_r}{R_r} + Z_0 C_c\left(1 - x^2\omega_0^2 L_r C_r\right)\right)} \tag{B.4}$$

The aim is to express the resonator impedance in terms of the internal and external quality factors as well as the resonance frequency. We can relate these to the circuit elements

$$Q_i = \omega_0 R_r (C_r + C_c) \tag{B.5}$$

$$Q_e = \frac{C_r + C_c}{Z_0 C_c^2 \omega_0} \tag{B.6}$$

$$S_{11} = \frac{1 - x^2 + ix\left(\frac{\omega_0^2 L_r (C_r + C_c)}{Q_i} + \frac{x^2 C_r - (C_r + C_c)}{C_c Q_e}\right)}{1 - x^2 + ix\left(\frac{\omega_0{}^2 L_r (C_r + C_c)}{Q_i} + \frac{(C_r + C_c) - x^2 C_r}{C_c Q_e}\right)} \tag{B.7}$$

Next, we introduce the coupling parameter as the ratio of the coupling capacitance to the total capacitance $\kappa = C_c/(C_r + C_c) \ll 1$ and emphasize that the frequency is in close vicinity from the resonator frequency

$$\omega = \omega_0 + \delta\omega \tag{B.8}$$

$$S_{11} = \frac{1 - \left(1 + 2\frac{\delta\omega}{\omega_0}\right) + i\left(1 + \frac{\delta\omega}{\omega_0}\right)\left(\frac{1}{Q_i} - \frac{1 - (1-\kappa)\left(1 + 2\frac{\delta\omega}{\omega_0}\right)}{\kappa Q_e}\right)}{1 - \left(1 + 2\frac{\delta\omega}{\omega_0}\right) + i\left(1 + \frac{\delta\omega}{\omega_0}\right)\left(\frac{1}{Q_i} + \frac{1 - (1-\kappa)\left(1 + 2\frac{\delta\omega}{\omega_0}\right)}{\kappa Q_e}\right)} =$$

$$= \frac{-2\frac{\delta\omega}{\omega_0} + i\left(\frac{1}{Q_i} - \frac{1}{Q_e} + \frac{2(1-\kappa)\frac{\delta\omega}{\omega_0}}{\kappa Q_e}\right) + i\left(\frac{\frac{\delta\omega}{\omega_0}}{Q_i} - \frac{\frac{\delta\omega}{\omega_0}}{Q_e} + \frac{2(1-\kappa)\left(\frac{\delta\omega}{\omega_0}\right)^2}{\kappa Q_e}\right)}{-2\frac{\delta\omega}{\omega_0} + i\left(\frac{1}{Q_i} + \frac{1}{Q_e} - \frac{2(1-\kappa)\frac{\delta\omega}{\omega_0}}{\kappa Q_e}\right) + i\left(\frac{\frac{\delta\omega}{\omega_0}}{Q_i} + \frac{\frac{\delta\omega}{\omega_0}}{Q_e} - \frac{2(1-\kappa)\left(\frac{\delta\omega}{\omega_0}\right)^2}{\kappa Q_e}\right)} \tag{B.9}$$

Now, we multiply with $-\omega_0/2$ and assume small frequency detuning

$$\kappa Q_i, \kappa Q_e \gg 1 \tag{B.10}$$

$$S_{11} = \frac{\delta\omega - i\left(\frac{\omega_0}{2Q_i} - \frac{\omega_0}{2Q_e} + \frac{(1-\kappa)\delta\omega}{\kappa Q_e}\right) - i\left(\frac{\delta\omega}{2Q_i} - \frac{\delta\omega}{2Q_e} + \frac{(1-\kappa)\frac{\delta\omega^2}{\omega_0}}{\kappa Q_e}\right)}{\delta\omega - i\left(\frac{\omega_0}{2Q_i} + \frac{\omega_0}{2Q_e} - \frac{(1-\kappa)\delta\omega}{\kappa Q_e}\right) - i\left(\frac{\delta\omega}{2Q_i} + \frac{\delta\omega}{2Q_e} - \frac{(1-\kappa)\frac{\delta\omega^2}{\omega_0}}{\kappa Q_e}\right)} \approx$$

$$\approx \frac{\delta\omega - i\left(\frac{\omega_0}{2Q_i} - \frac{\omega_0}{2Q_e}\right)}{\delta\omega - i\left(\frac{\omega_0}{2Q_i} + \frac{\omega_0}{2Q_e}\right)} \tag{B.11}$$

Finally, we can introduce the linewidths (damping rates) associated with the two quality factors $\Gamma_{i,e} = \omega_0/(2\pi Q_{i,e})$ and express the reflection coefficients on the form

$$S_{11} = \frac{\delta f^2 + \frac{1}{4}\left(\Gamma_i^2 - \Gamma_e^2\right) + i\Gamma_e \delta f}{\delta f^2 + \frac{1}{4}\left(\Gamma_i + \Gamma_e\right)^2} \tag{B.12}$$

The magnitude and phase of the reflection coefficient are thus

$$|S_{11}| = \sqrt{\mathrm{Re}\left[S_{11}\right]^2 + \mathrm{Im}\left[S_{11}\right]^2} = \frac{\sqrt{\left[\delta f^2 + \frac{1}{4}\left(\Gamma_i^2 - \Gamma_e^2\right)\right]^2 + \left[\Gamma_e \delta f\right]^2}}{\delta f^2 + \frac{1}{4}\left(\Gamma_i + \Gamma_e\right)^2} \tag{B.13}$$

$$\arg\left(S_{11}\right) = \arctan\left(\frac{\mathrm{Im}\left[S_{11}\right]}{\mathrm{Re}\left[S_{11}\right]}\right) = \arctan\left(\frac{\Gamma_e \delta f}{\delta f^2 + \frac{1}{4}\left(\Gamma_i + \Gamma_e\right)^2}\right) \tag{B.14}$$

Appendix C

Conformal mapping

To simulate the inductance and capacitance per unit length we use conformal mapping[53], where the electric field lines between the center conductor and ground planes are mapped onto those of a parallel plate capacitor. The dielectric environment of the sample layers is taken into account by deriving a capacitance assosiated with each dielectric layer. In this section, we go through the equations used to simulate the characteristic impedance.

We start out from the capacitance of the partial dielectric regions, C_1 and C_2 is expressed as

$$C_i = 2\epsilon_0 \left(\epsilon_{r,i} - 1\right) \frac{K(k_i)}{K(k_i')}, \tag{C.1}$$

where ϵ_0 and $\epsilon_{r,i}$ are the vacuum and relative perimittivity, respectively, and K denotes elliptic integrals with modulus, k_i and k_i', defined as

$$k_i = \frac{\sinh\left(\pi w/4h_i\right)}{\sinh\left(\pi(w+2g)/4h_i\right)} \qquad k_i' = \sqrt{1-k_i} \qquad i \in [1,2], \tag{C.2}$$

where w and g are the widths of the center conductor and gaps, respectively. Next, the capacitive contribution from the vacuum in absence of the dielectric layers below the conductor is given by

$$C_{\text{vac}} = 2\epsilon_0 \left[\frac{K(k_3)}{K(k_3')} + \frac{K(k_4)}{K(k_4')}\right] \tag{C.3}$$

with corresponding modulus

$$k_j = \frac{\tanh\left(\pi w/4h_j\right)}{\tanh\left(\pi(w+2g)/4h_j\right)} \qquad k_j' = \sqrt{1-k_j} \qquad j \in [3,4]. \tag{C.4}$$

We can now define an effective dielectric constant

$$\epsilon_{\text{eff}} = 1 + q_1(\epsilon_{r,1} - 1) + q_2(\epsilon_{r,2} - 1) \tag{C.5}$$

where q_1 and q_2 are the partial filling factors, defined as

$$q_i = \frac{K(k_i)}{K(k_i')} \left[\frac{K(k_3)}{K(k_3')} + \frac{K(k_4)}{K(k_4')} \right]^{-1} \qquad i \in [1, 2] \tag{C.6}$$

Moreover, the phase velocity and characteristic impedance can be expressed in terms of the effective dielectric constant

$$v_{\text{ph}} = \frac{c}{\sqrt{\epsilon_{\text{eff}}}} \tag{C.7}$$

$$Z_c = \frac{1}{c C_{\text{vac}} \sqrt{\epsilon_{\text{eff}}}} = \frac{60\pi}{\sqrt{\epsilon_{\text{eff}}}} \left[\frac{K(k_3)}{K(k_3')} + \frac{K(k_4)}{K(k_4')} \right]^{-1} \tag{C.8}$$

Inductance and capacitance per unit length

After calculating the cross section geometry, we can use the same conformal mapping to obtain information about the inductance and capacitance per unit length of the coplanar waveguide transmission line

$$L = \frac{\mu_0}{2} \left[\frac{K(k_3)}{K(k_3')} + \frac{K(k_4)}{K(k_4')} \right]^{-1} \tag{C.9}$$

$$C = 2\epsilon_0 \epsilon_{\text{eff}} \left[\frac{K(k_3)}{K(k_3')} + \frac{K(k_4)}{K(k_4')} \right]^{-1} \tag{C.10}$$

Bibliography

[1] R. P. Feynman, "Simulating Physics with Computers", *Int. Jour. of Th. Phys.* **21**: 467-488 (1982)

[2] A. Blais, R.-S. Huang, A. Wallraff, S.M. Girvin, and R. J. Schoelkopf, "Cavity quantum electrodynamics for superconducting electrical circuits: An architecture for quantum computation", *Phys. Rev. A*, **69** 062320 (2004)

[3] A. Wallraff, D. I. Schuster, A. Blais, L. Frunzio, R. S. Huang, J. Majer, S. Kumar, S. M. Girvin, and R. J. Schoelkopf, "Strong coupling of a single photon to a superconducting qubit using circuit quantum electrodynamics", *Nature*, **431** 162 (2004)

[4] K. H. Onnes, "The Superconductivity of Mercury", *Comm. Phys. Lab. Univ. Leiden* **122**, 251 (1911)

[5] R. P. Feynman, *Lectures on physics Vol III*, Pearson Addison-Wesley, (2006)

[6] M. Tinkham, *Introduction to superconductivity*, 2$^{\text{nd}}$ edition, Dover Publications Inc., (2004)

[7] T. van Duzer, and C. W. Turner, *Principles of superconductive devices and circuits*, Prentice Hall PTR, 2$^{\text{nd}}$ edition, (1999)

[8] J. Bardeen, L. N. Cooper, and J. R. Schrieffer, "Theory of superconductivity", *Phys. Rev.* **108**, 1175 (1957)

[9] B. D. Josephson, "Possible new effects in superconductive tunnelling", *Phys. Lett.* **1**, 251 (1962)

[10] C. P. Wen, "Coplanar Waveguide: A Surface Strip Transmission Line Suitable for Nonreciprocal Gyromagnetic Device Applications", *IEEE Transactions on Microwave Theory and Techniques*, **MTT-17** 12 (1969)

[11] D. M. Pozar, *Microwave engineering*, John Wiley and sons, inc., 3$^{\text{rd}}$ edition, (2005)

[12] K. Watanabe, K. Yoshida, T. Aoki, and S. Kohjiro, "Kinetic inductance of superconducting coplanar waveguides", *Jpn. J. Appl. Phys.* **33**, pp. 5708-5712 (1994)

[13] P. A. M. Dirac, "The quantum theory of the emission and absorption of radiation", *Proc. Roy. Soc.* **A114**, 243 (1927)

[14] A. Einstein, "Strahlungs-emission und -absorption nach der quantentheorie", *Verhandlungen der Deutschen Physikalischen Gesellschaft*, **18**, 318-323 (1916)

[15] S-I. Tomonaga, "On a relativistic invariant formulation of the quantum theory of wave fields", *Progress of Theoretical Physics* **1**, 27 (1946)

[16] J. Schwinger, "On quantum-electrodynamics and the magnetic moment of the electron", *Phys. Rev.* **73**, 416 (1948)

[17] R. P. Feynman, "Space-time approach to non-relativistic quantum mechanics", *Rev. Mod. Phys.* **20**, 367 (1948)

[18] S. Haroche, and D. Kleppner, "Cavity quantum electrodynamics", *Physics Today*, **42**, 24 (1989)

[19] S. Haroche, and J-M. Raimond, *Exploring the Quantum: Atoms, Cavities, and Photons*, Oxford University Press Inc., New York, USA, (2006)

[20] S. Wahlsten, S. Rudner, and T. Claeson, "Parametric amplification in arrays of Josephson tunnel junctions", *Appl. Phys. Lett.*, **30**, 298 (1977)

[21] M. Wallquist, V. S. Shumeiko, and G. Wendin, "Selective coupling of superconducting charge qubits mediated by a tunable stripline cavity", *Phys. Rev. B* **74**, 224506 (2006)

[22] M. A. Castellanos-Beltran, and K. W. Lehnert, "Widely tunable parametric amplifier based on a superconducting quantum interference device array resonator", *Appl. Phys. Lett.*, **91** 083509, (2007)

[23] T. Yamamoto, K. Inomata, M. Watanabe, K. Matsuba, T. Miyazaki, W. D. Oliver, Y. Nakamura, and J. S. Tsai, "Flux-driven Josephson parametric amplifier", *Appl. Phys. Lett.*, **93** 042510, (2008)

[24] M. Sandberg, C. M. Wilson, F. Persson, T. Bauch, G. Johansson, V. Shumeiko, T. Duty, and P. Delsing, "Tuning the field in a microwave resonator faster than the photon lifetime", *Appl. Phys. Lett.*, **92** 203501, (2008)

[25] J. Koch, T. M. Yu, J. Gambetta, A. A. Houck, D. I. Schuster, J. Majer, A. Blais, M. H. Devoret, S. M. Girvin, and R. J. Schoelkopf, "Charge-insensitive qubit design derived from the Cooper pair box", *Phys. Rev. A* **76**, 042319 (2007)

[26] M. Büttiker, "Role of quantum coherence in series resistors", *Phys. Rev. B* **33**, 3020 (1986)

[27] Y. Nakamura, Y. A. Pashkin, and J. S. Tsai, "Coherent control of macroscopic quantum states in a single-Cooper-pair box", Nature **398**, (1999)

[28] K. Bladh, T. Duty, D. Gunnarsson, and P. Delsing, "The single Cooper-pair box as a charge qubit", *New Journal of Physics*, **7**, 180, (2005)

[29] A. R. Lide, *Handbook of chemistry and physics*, CRC Press LLC, 85^{th} edition, (2004)

[30] D. Vion, A. Aassime, A. Cottet, P. Joyez, H. Pothier, C. Urbina, D. Esteve, and M. H. Devoret, "Manipulating the quantum state of an electrical circuit", *Science* **296**, 886 (2002)

[31] T. van Duzer, C.W. Turner *Principles of superconductive devices and circuits*, Prentice Hall PTR, 2^{nd} edition, (1999)

[32] E. T. Jaynes and F. W. Cummings, "Comparison of quantum and semiclassical radiation theories with application to the beam maser", *Proc. IEEE* **51** (1): 89-109, (1963)

[33] C. C. Gerry and P. L. Knight, *Introductory Quantum Optics*, Cambridge University Press, Cambridge, England, (2005)

[34] M. Faraday, Philosophical Transactions of the Royal Society (London), vol. **121**, pages 299-318. (1831)

[35] B. Yurke, P. G. Kaminsky, R. E. Miller, E. A. Whittaker, A. D. Smith, A. H. Silver, and R. W. Simon, "Observation of 4.2-K equilibrium-noise squeezing via a Josephson parametric amplifier", *Phys. Rev. Lett.*, **60**, 764-767 (1988)

[36] B. Yurke, L. R. Corruccini, P. G. Kaminsky, L. W. Rupp, A. D. Smith, A. H. Silver, R. W. Simon, and E. A. Whittaker, "Observation of parametric amplification and deamplification in a Josephson parametric amplifier", *Phys. Rev. A*, **39**, 2519 (1989)

[37] L. D. Landau and E. M. Lifshitz, *Mechanics, vol. 1 (3rd ed.)*, Pergamon Press, (1976)

[38] C. M. Wilson, T. Duty, M. Sandberg, F. Persson, V. Shumeiko, and P. Delsing, "Photon generation in an electromagnetic cavity with a time-dependent boundary", *Phys. Rev. Lett.* **105**, 233907 (2010)

[39] A. Palacios-Laloy, F. Nguyen, F. Mallet, P. Bertet, D. Vion, and D. Esteve, "Tunable resonators for quantum circuits", *J. Low Temp. Phys.*, **151** (1034-42), (2008)

[40] Wilson, C. M., Duty, T., and Delsing, P. *Fluctuating Nonlinear Oscillators*, Edited by M. Dykman, Oxford Univ. Press, (2012)

[41] B. Yurke, J. S. Denker, "Quantum network theory", *Phys. Rev. A*, **29**(3), 1419-1437 (1984)

[42] M. H. Devoret, *Les Houches, session LXIII*, Elsevier Science, (1995)

[43] S. H. Strogatz, *Nonlinear dynamics and chaos*, Addison-Wesley Publishing Company, USA (1994)

[44] M. Dykman, "Fluctuational phase-flip transitions in parametrically driven oscillators", *Phys. Rev. E*, **57**, 5202 (1998)

[45] G. J. Dolan, "Offset masks for lift-off photoprocessing", *Appl. Phys. Lett.*, **31**, 337 (1977)

[46] R. N. Simons, *Coplanar Waveguide Circuits, Components, and Systems*, **John Wiley & Sons**, (2001)

[47] F. Mallet, F. R. Ong, A. Palacios-Laloy, F. Nguyen, P. Bertet, D. Vion, and D. Esteve, "Single-shot qubit readout in circuit quantum electrodynamics", *Nature Physics* **5**, 791-795 (2009)

[48] V. E. Manucharyan, E. Boaknin, M. Metcalfe, R. Vijay, I. Siddiqi, and M. Devoret, "Microwave bifurcation of a Josephson junction: Embedding-circuit requirements", *Phys. Rev. B*, **76** (014524), (2007)

[49] P. Bertet, F. R. Ong, M. Boissonneault, A. Bolduc, F. Mallet, A. C. Doherty, A. Blais, D. Vion, and D. Esteve, *Fluctuating Nonlinear Oscillators*, Edited by M. Dykman, Oxford University Press, (2012)

[50] W. Wustmann, and V. S. Shumeiko, "Parametric resonance in tunable superconducting cavities", *Phys. Rev. B*, **87**, 184501 (2013)

[51] K. Sundquist, S. Kintaş, M. Simoen, P. Krantz, M. Sandberg, C.M. Wilson, and P. Delsing, "The pumpistor: a linearized model of a flux-pumped superconducting quantum interference device for use as a negative-resistance parametric amplifier", *Appl. Phys. Lett.* **103**, 102603 (2013)

[52] P. Krantz, Y. Reshitnyk, W. Wustmann, J. Bylander, S. Gustavsson, W. D. Oliver, T. Duty, V. Shumeiko, and P. Delsing, "Investigation of nonlinear effects in Josephson parametric oscillators used in circuit QED", *New. Jour. of Phys.* **15**, in press (2013)

[53] N. S. Rainee, *Coplanar Waveguide Circuits, Components, and Systems*, John Wiley & Sons, New York, USA, (2001)